

Celina Grabowska

# **3D CITY MODEL VALIDATION USING GNSS SIGNALS**

Master of Science Thesis  
Faculty of Information Technology and Communication Sciences  
Examiners: DSc (Tech) Philipp Müller  
and DSc (Tech) Helena Leppäkoski  
August 2020

# ABSTRACT

Celina Grabowska: 3D city model validation using GNSS signals  
Master of Science Thesis  
Tampere University  
Data Engineering and Machine Learning  
August 2020

---

3D city models provide three-dimensional representation of city areas and are used in visualization, navigation, urban planning and many others. For example, they are employed in positioning algorithms such as shadow matching that improves accuracy in urban areas. Correctness of the 3D models is essential so that validation methods are needed. GNSS observations carry information about receiver surroundings and could be used for that purpose. Furthermore, GNSS data can be crowd sourced which would provide huge amount of data with broad coverage.

GNSS signals are affected by different types of obstacles before reaching receivers. In urban areas the most common obstacles are high buildings. These obstacles can cause significant signal deterioration. They can cause signal attenuation, blockage or multipath. All those negative effects are reflected in GNSS measurements. For example, significant changes in the signal-to-noise ratio can indicate that a signal is being blocked.

On the other hand, given a 3D model of the buildings in an area, it is possible to predict the behavior of GNSS signals. It is, for example, possible to estimate whether a signal at a certain location is going to be shadowed by a building or not.

By comparing which signals are shadowed according to GNSS observations and 3D model-based estimations, it is possible to detect errors in 3D maps. For instance, if GNSS measurements show blocked signals and corresponding 3D model-based predictions do not it can indicate lack of a building in a model. Extra elements in the model such as new buildings or added floors can be detected as well.

The goal of the thesis is to use GNSS observations for the validation of a 3D city map. Detected errors can provide information which areas need to be investigated and possibly re-mapped. Moreover, everyday use devices such as smartphones, watches, cars, etc. are equipped in GNSS receivers. It opens an opportunity for crowd sourcing. However, those low-cost, consumer-grade receivers have significantly lower quality than professional devices. Therefore, the second objective is to examine the feasibility of using smart devices as a source of GNSS data.

The thesis includes the analysis of the GNSS observations collected with smartphones and a professional receiver. The data was collected from locations with newly built buildings that were not yet included in the model. Moreover, the algorithm comparing GNSS and 3D model based predictions of blocked signals is presented. The results confirmed the validity of the concept. However, the errors in the 3D map were detected only using the professional receiver. The data collected with smartphones did not provide enough information and so was not enough to detect the errors.

Keywords: GNSS, 3D city models, Smartphones

The originality of this thesis has been checked using the Turnitin OriginalityCheck service.

## **PREFACE**

The thesis was commissioned by HERE Technologies. Many thanks to Stefan Söderholm and Saara Kuusmanen for supervising my work and guiding me through the process. Also to my manager Jyrki Aarnos and my team for great work environment and knowledge sharing. Special word of thanks to supervisors from the Tampere University, DSc (Tech) Helena Leppäkoski and DSc (Tech) Philipp Müller, for instructions and constructive feedback. Working with all of you was a priceless and growing experience.

Tampere, 1st August 2020

Celina Grabowska

# CONTENTS

1	Introduction . . . . .	1
2	Satellite navigation . . . . .	3
2.1	Satellite Navigation . . . . .	3
2.2	Reference systems . . . . .	5
2.2.1	Coordinate reference systems . . . . .	5
2.2.2	Time reference systems . . . . .	5
2.3	Navigation Data . . . . .	6
2.4	Satellite signals . . . . .	6
2.4.1	Radio signals basics . . . . .	6
2.4.2	Frequency Bands . . . . .	7
2.4.3	Wave propagation . . . . .	7
2.4.4	Satellite signal composition . . . . .	9
3	GNSS measurements . . . . .	10
3.1	Receivers . . . . .	10
3.2	Observables . . . . .	11
3.3	Signal strength . . . . .	12
3.4	GNSS receivers in smartphones . . . . .	13
3.5	Android raw measurements . . . . .	14
4	Disruptions . . . . .	16
4.1	Interference . . . . .	16
4.2	Signal blockage . . . . .	16
4.3	Multipath . . . . .	17
4.4	Shadow matching . . . . .	17
5	Data analysis . . . . .	19
5.1	Data collection . . . . .	19
5.2	Data processing . . . . .	20
5.2.1	3D-model based predictions . . . . .	22
5.2.2	GNSS-based predictions . . . . .	24
5.3	Reality Index . . . . .	27
6	Conclusions . . . . .	39
	References . . . . .	41

## LIST OF FIGURES

2.1	Architecture of a satellite navigation system (source: [6]). . . . .	4
2.2	Electromagnetic spectrum (source: [4, p. 60]). . . . .	8
2.3	Reflection and refraction of an electromagnetic wave (source: [4, p. 61]. . .	8
2.4	Signal composition (source: [4, p. 55]). . . . .	9
3.1	GNSS receiver (source: [4, p. 85]). . . . .	10
4.1	Signal blockage (source [12]). . . . .	17
4.2	Multipath (source [12]). . . . .	17
4.3	Shadow matching (source [1]). . . . .	18
5.1	Device installation. . . . .	20
5.2	Block diagram of data processing. . . . .	21
5.3	Satellite's azimuth and elevation (source [22]). . . . .	22
5.4	Building represented with a triangle mesh. . . . .	23
5.5	3D model-based predictions of blocked angles at a certain path point. . . .	24
5.6	Comparison of mean $C/N_0$ values from smartphones and NovAtel for dif- ferent elevation angles. . . . .	25
5.7	Comparison of mean $C/N_0$ values of different GPS satellites. . . . .	25
5.8	Skyplots in a reference location in Tampere (source [25]). . . . .	26
5.9	$C/N_0$ values of GPS21 satellite over collection time. . . . .	27
5.10	$C/N_0$ values of GPS5 satellite over collection time. . . . .	28
5.11	Division of the sky view. . . . .	29
5.12	Reality Index based on the NovAtel log file. . . . .	30
5.13	Satellite images of discussed areas in the left column (source [26]) and their corresponding 3D models in the right column. . . . .	33
5.14	Sky plots comparing 3D model and GNSS based predictions from the No- vAtel in discussed locations. . . . .	35
5.15	Reality Index based on the smartphone log file. . . . .	36
5.16	Sky plots comparing 3D model and GNSS based predictions from the smartphone in discussed locations. . . . .	37
5.17	Reality Index based on combined NovAtel's log files. . . . .	38
5.18	Reality Index based on combined smartphones' log files. . . . .	38

## LIST OF TABLES

2.1	Satellite constellations. . . . .	3
5.1	Software and data formats. . . . .	22
6.1	Summary of errors detection . . . . .	39

## LIST OF SYMBOLS AND ABBREVIATIONS

$C/N_0$	Carrier-to-noise ratio
$A$	Amplitude
A-GNSS	Assisted-GNSS
$\beta_i$	Angle of incidence
$\beta_r$	Angle of refraction
DSP	Digital Signal Processor
ECEF	Earth-centered, Earth-fixed
ECI	Earth-centered inertial
ECR	Earth-centered rotational
ETRS-GK24FIN	ETRS Finland
ETRS89	European Terrestrial Reference System 1989
$f$	Frequency
FBX	Filmbox file format
GIS	Geographic Information System
GLONASS	GLObal NAvigation Satellite System
GNSS	Global Navigation Satellite Systems
GPS	Global Positioning System
GPST	GPS time
GPX	GPS Exchange Format
$Hz$	Hertz
IGS	International GNSS Service
ITU	International Telecommunication Union
$L$	Transmission loss
L1	Link 1 frequency
L2	Link 2 frequency
LOS	Line-of-sight
MCS	Master Control Station
MEO	Medium Earth orbit
$n_i, n_r$	Refraction indices of mediums

NASA	The National Aeronautics and Space Administration
NavIC	Navigation with Indian Constellation
NLOS	Non-line-of-sight
$\varphi$	Phase
PPP	Precise Point Positioning
$P_r$	Power of the signal received by a receiver
PRN	Pseudorandom Noise
$P_s$	Power of the signal emitted by a satellite
QZSS	Quasi-Zenith Satellite System
RF	Radio front-end
RINEX	Receiver Independent Exchange Format
RTK	Real Time Kinematic
SATNAV	Satellite Navigation
SNR	Signal-to-noise ratio
SPAN	Synchronized Position Attitude Navigation
SV	Space Vehicle
$t$	Time
TAI	International Atomic Time
TIREM	Terrain-Integrated Rough-Earth Model
TOA	Time of arrival
TTFF	Time to first fix
UT	Universal Time
UT1	Universal Time version 1
UTC	Coordinated Universal Time
WGS84	World Geodetic System

# 1 INTRODUCTION

Navigation signals transmitted by satellites are affected by different types of obstacles before reaching receivers. In urban areas the most common obstacles are high buildings. These obstacles can cause significant signal deterioration in the form of signal attenuation, blockage or multipath. All those negative effects are reflected in the receiver's measurements. For example, signal power significantly drops when the signal is being blocked. Hence, based on the signal power value we can recognize blocked signals.

On the other hand, given a 3D model of the buildings in an area, it is possible to predict satellite signal propagation. For example, it is possible to estimate whether the incoming signal at a certain location intersects with objects surrounding the receiver and so if it is going to be shadowed by a building or not.

In [1] 3D models were used to improve positioning accuracy in urban environments. High buildings along streets form urban canyons where across-street positioning is especially challenging. It is caused by the fact that satellite signals going across a street are much more likely to be blocked. The across-street signals perpendicularly intersect the street. Based on a 3D city map authors predicted satellite visibility. It was shown that comparison of predicted and measured satellite visibility can be used to determine more accurate location. Authors' solution significantly enhanced across-street accuracy.

Comparing predictions of blocked signals based on 3D model and satellite observations can be also used to validate whether the 3D model is up to date. For example, non-matching predictions can indicate that a newly built building has not been added to the model yet or that a demolished building has not been removed from the model yet.

In addition, mobile devices (e.g. smartphones, tablets, laptops) equipped with satellite navigation receivers create a good opportunity for crowd sourcing of satellite observations that could be used for the 3D model validation. Crowd sourced observations could provide huge amount of data and a global coverage. However, the receivers in the above-mentioned, consumer-grade devices are often low-cost and observation quality is significantly worse than that of professional devices as stated in [2]. One of the aims of this work is to investigate the feasibility to use crowd sourced GNSS observations from such devices for validation of 3D city maps. In [3] crowd sourced data from mobile devices was used to detect and characterize buildings in 3D. Authors transformed a set of satellites signals into a 3D representation of the space they crossed. As a result, it was possible to construct 3D buildings. It was proven that crowd sourced, low quality data collected in an

uncontrolled manner is sufficient for that purpose.

Goals of the thesis are to validate the 3D city model using GNSS raw observations and verify whether mobile devices can provide sufficient data for this purpose. To demonstrate thesis concept the following test was carried out. Raw satellite observations from smartphones and high-end NovAtel receiver were collected in the city of Tampere. The data collection route included places with new buildings, not present in the 3D map of the city. Then, an algorithm comparing 3D-model and GNSS based predictions was implemented. Its task was to detect missing elements in the model. Next, comparison of the data quality from smartphones and NovAtel was made.

The thesis includes the analysis of carrier-to-noise ratio measurements from smartphones and the NovAtel receiver. Moreover, the algorithm detecting errors in a 3D model using raw GNSS observations was proposed and evaluated based on collected data. The algorithm detected missing and extra elements in the model. However, some detected errors were false. Furthermore, the algorithm was prone to the negative effect of multipath and the relatively small data set of smartphone observations was insufficient to prove the usability of smartphones' receivers.

The thesis is structured in the following way. The second chapter introduces the basic concepts of the satellite navigation systems. The system architecture, reference systems, and satellite signals are described. The third chapter focuses on GNSS measurements and receivers. In addition, it covers the specification of smartphone receivers and Android raw measurements. In the fourth chapter signals disruptions are described. Further, the fifth chapter is devoted to data analysis. The description of carried out tests is included as well as the explanation of the applied algorithm and its results. Finally, chapter six provides the summary of the work and possible, future research.

## 2 SATELLITE NAVIGATION

In this chapter, basic concepts of satellite navigation and satellite signals are described. This chapter is based on books [4] and [5].

### 2.1 Satellite Navigation

Satellite Navigation (SATNAV) systems provide continuous position, velocity and time information for users around the world. A network of satellites orbiting the Earth broadcasts radio signals that enable receiving devices to determine their positions. There are several SATNAV systems operating globally or locally. The four Global Navigation Satellite Systems (GNSS) are GPS, GLONASS, Galileo, and BeiDou, and the two regional systems are NavIC and QZSS. Table 2.1 summarizes the characteristics of these systems such as the owner of the system, year of the launch, coverage, approximate altitude of orbit planes in kilometers, and orbital periods in hours.

The best known and oldest GNSS system, operated by the United States, is GPS which stands for Global Positioning System. Further description of system architecture and principles of operation are based on GPS. Nonetheless, the majority of this information is common to all SATNAVs. Knowledge of one system helps in understanding the others and is sufficient for purposes of this work.

The architecture of the navigational system is divided into three parts: space, control and user segment. The architecture is illustrated in Figure 2.1.

The space segment is a set of satellites, which are also called space vehicles (SVs). The satellites of one navigational system form a constellation. GPS nominally consists of 24 SVs in 6 medium altitude earth orbits ( $\approx 20000$  km). However, there are six SV slots per

**Table 2.1.** *Satellite constellations.*

system	owner	year	coverage	altitude (km)	period (h)
GPS	USA	1978	global	20,180	11.97
GLONASS	Russia	1982	global	19,130	11.26
Galileo	EU	2011	global	23,222	14.08
BeiDou	China	2015	global	21,150	12.63
NavIC	India	2018	regional	36,000	23.93
QZSS	Japan	2018	regional	32,600	23.93

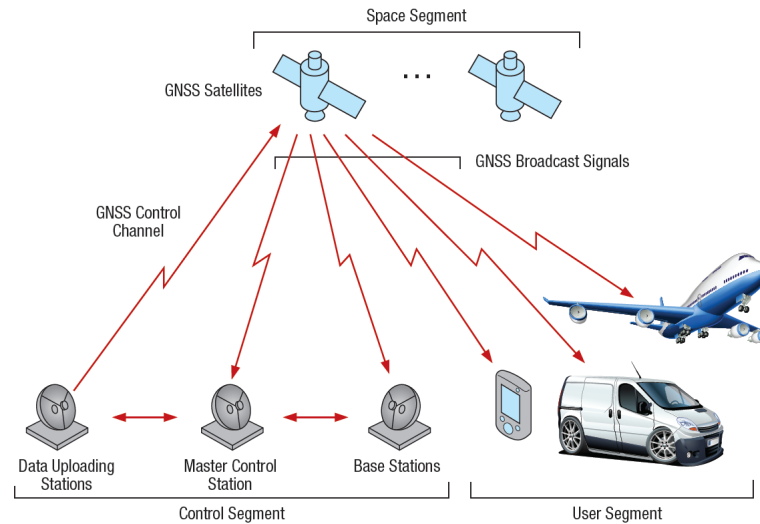


**Figure 2.1.** Architecture of a satellite navigation system (source: [6]).

orbital plane so there is space for more satellites. The satellites are equally spaced so there are four satellites per orbital plane. The orbital period (the time in which a satellite travels the whole orbit once) of a GPS satellite is 11 hours and 58 minutes and the orbital radius is approximately 26,600 km. This baseline 24-slot constellation system can provide continuous global service and at least 4 satellites in range of a receiver in any place on Earth. GPS is a one-way, downlink (space-to-earth) system, which means that satellites constantly emit signals and an unlimited number of users receive them simultaneously. The satellites transmit Pseudorandom Noise (PRN) coded signals. Additionally, each satellite has a unique PRN code so that receivers can distinguish from which SV the signal was received. It allows many satellites to broadcast signals in the same frequency band.

The control segment is comprised of ground stations that control and monitor satellites' operations. The elements of the control segment are Master Control Station (MCS), monitor stations and ground antennas. In Figure 2.1 monitor stations and ground antennas are called base stations and data uploading stations respectively. Monitor stations track all satellites and transmit measurements to master control station. MCS monitors and maintains orbits and satellite health. Furthermore, it maintains time parameters, computes satellite locations and generates navigational data. Ground antennas send commands to the satellites and upload navigational messages.

The user segment is made up of all devices receiving satellite signals. Thanks to the great advancement in integrated circuits, which are now compact and light, GNSS receivers are included in many devices such as smartphones, smartwatches, cameras, cars, etc. Receivers calculate their position based on navigation data from satellites using the concept of Time of arrival (TOA) ranging. It is a fundamental concept of satellite navigation. The time that it takes for a signal transmitted by a satellite to reach a receiver is called the propagation time. In principle, multiplying that time by the speed of signal propagation gives the distance it traveled. Knowing the distance to transmitter at a known location

allows to determine receiver position.

## 2.2 Reference systems

Satellite navigation requires a common coordinate reference system and time reference system to describe position and velocity vectors of satellites and receivers.

### 2.2.1 Coordinate reference systems

The Earth-centered inertial (ECI) coordinate system origins at the center of mass of the Earth and does not rotate with respect to the stars. Therefore, it is especially convenient to describe objects in space. The x–y plane coincides with the equatorial plane of Earth. The x-axis is fixed in a particular direction relative to the celestial sphere, and does not rotate along with the Earth. The z-axis is perpendicular to the equatorial plane and crosses the North Pole.

For describing terrestrial objects it is more common to use the Earth-centered, Earth-fixed (ECEF) system, also known as Earth-centered rotational (ECR). In this system the x-axis (pointing in the direction of  $0^\circ$  longitude) and the y-axis (pointing in the direction of  $90^\circ$  East longitude) rotate with the Earth. The x–y plane is coincident with the equatorial plane. The perpendicular z-axis extends through the true North. In this system positions are described as (X, Y, Z) coordinates and the point (0, 0, 0) is defined as the center of mass of the Earth. The Cartesian (X, Y, Z) coordinates can be converted to geodetic coordinates (latitude, longitude, height). For example, the method presented in [7] provides an approximate transformation from ECEF coordinates to geodetic coordinates. It is an iterative approach using the Newton-Raphson method. It proved to have a good efficiency and accuracy.

In order to unambiguously indicate a location on the Earth a reference ellipsoid must be defined. The reference ellipsoid is a mathematical approximation of the geoid's surface. The whole Earth is best described by a different ellipsoid than an ellipsoid describing only its part. Therefore, global and local geodetic datums were created. A geodetic datum defines a reference ellipsoid and a coordinate system that are used to define locations. An example of a global datum is the World Geodetic System (WGS84), which is a default datum used by GPS. Another example is the European Terrestrial Reference System 1989 (ETRS89), which represents Europe as a static plane and is robust to changes caused by the continental drift. Even more specific datum is the ETRS-GK24FIN which particularly covers Finland.

### 2.2.2 Time reference systems

There are several time systems associated with different periodic process such as Earth rotation, Earth resolution, and atomic oscillations. Universal Time (UT) is a time system

based on Earth's rotation. Its primary form is UT1 that is based on the mean solar time at 0° longitude. However, Earth rotation is not uniform due to, for example, tidal frictions and mass transports. To compensate for the non-uniformity of the UT1 the International Atomic Time (TAI) system is used. TAI is a high-precision atomic time. The combination of TAI and UT1 forms Coordinated Universal Time (UTC). UTC is an atomic time and it is within about 1 second of UT1. It is achieved by systematically adding a certain number of leap seconds. Consequently, the UTC is not a continuous time system. All SATNAV systems heavily rely on time. It is crucial to keep all segments of the system synchronised. Hence, each SATNAV has its own time reference system. GPS time (GPST) is based on atomic clocks in MCS and SVs. It is regulated by the control segment and it is continuous.

## 2.3 Navigation Data

To determine its position a receiver needs accurate information about the positions of GNSS satellites. There are three data sets allowing to calculate positions and velocities of SVs: almanac data, broadcast ephemerides, and precise ephemerides. First, the almanac data, broadcasted in the satellite message, consists of coarse orbit and satellite status information. It is used at receiver's start up to detect satellites for the first time. The broadcast ephemerides contain more accurate data describing the location of satellites with respect to time. They are calculated by the monitor stations and uploaded to satellites that include them into the satellite message. The navigational message sent by satellites provides not only ephemeris and almanac but also clock parameters and satellite health status. The parameters are used to compute the precise satellite's clock taking into account any time errors and delays.

The precise ephemerides are the most accurate and are provided by International GNSS Service (IGS). They are not included in the navigational message but available to download from IGS servers. They consist of satellite positions and velocities at certain epochs.

## 2.4 Satellite signals

### 2.4.1 Radio signals basics

Satellite navigation relies on electromagnetic waves that can be represented by a sinusoidal wave characterized by:

$$y(t) = A \sin(2\pi ft + \varphi), \quad (2.1)$$

- A - amplitude
- f - linear frequency
- t - time parameter

- $\varphi$  - phase

The amplitude is the peak value of the wave. The linear frequency is the number of cycles occurring per second and is given in Hertz ( $Hz$ ). Phase tells where in its cycle the oscillation is at time zero and it is given in radians.

In case transmitter and receiver are in relative motion, as it happens with constantly moving satellites, the wave is affected by the Doppler effect. The Doppler effect is a frequency shift resulting in the received frequency higher than emitted from an approaching transmitter and lower than emitted from an receding transmitter. The Doppler shift is used as a measure for velocity or, after integration over time, it is proportional to range differences.

### 2.4.2 Frequency Bands

The International Telecommunication Union (ITU) regulates usage of frequency bands in the electromagnetic spectrum. Figure 2.2 shows the division of the spectrum. Different bands are allocated to different services. Satellite navigation systems have been allocated to the L-band (1-2 [GHZ]), S-band (2-4 [GHZ]), and C-band (4-8 [GHZ]). According to the original GPS design the system provides separate signals for civilian and military use. Civilian signals contain the coarse/acquisition (C/A) code while military signals contain the restricted precision (P) code. Furthermore, the original design utilize two frequencies that are referred to as the legacy signals. First called Link 1 frequency (L1) is at 1,575.42 MHz and the second called Link 2 frequency (L2) is at 1,227.6 MHz. The civilian signals use L1 and military signals use both L1 and L2. After GPS modernization there are now three new signals for civilian use: L2C, L5, and L1C which gives four civilian signals in total. Modernized military signals otherwise known as M code were added to L1 and L2.

### 2.4.3 Wave propagation

Electromagnetic waves are affected by several physical phenomena.

Reflection occurs when a wave meets a surface of a medium it is propagating through. The law of reflection states that the reflection angle equals the angle of incidence. The absolutely smooth surfaces result in a specular reflection while rough surfaces cause the reflection to be diffuse. In the latter case the energy of a wave is dispersed in various directions. It is a reason of an effect called multipath which means that the satellite signal is reflected or scattered before it reaches the receiver.

Refraction is the phenomenon of the change in the wave's propagation direction due to passing from one medium to another. According to Snell's law, 2.2, the sine of the angle of incidence,  $\beta_i$ , and the sine of the angle of refraction,  $\beta_r$ , define a constant ratio that

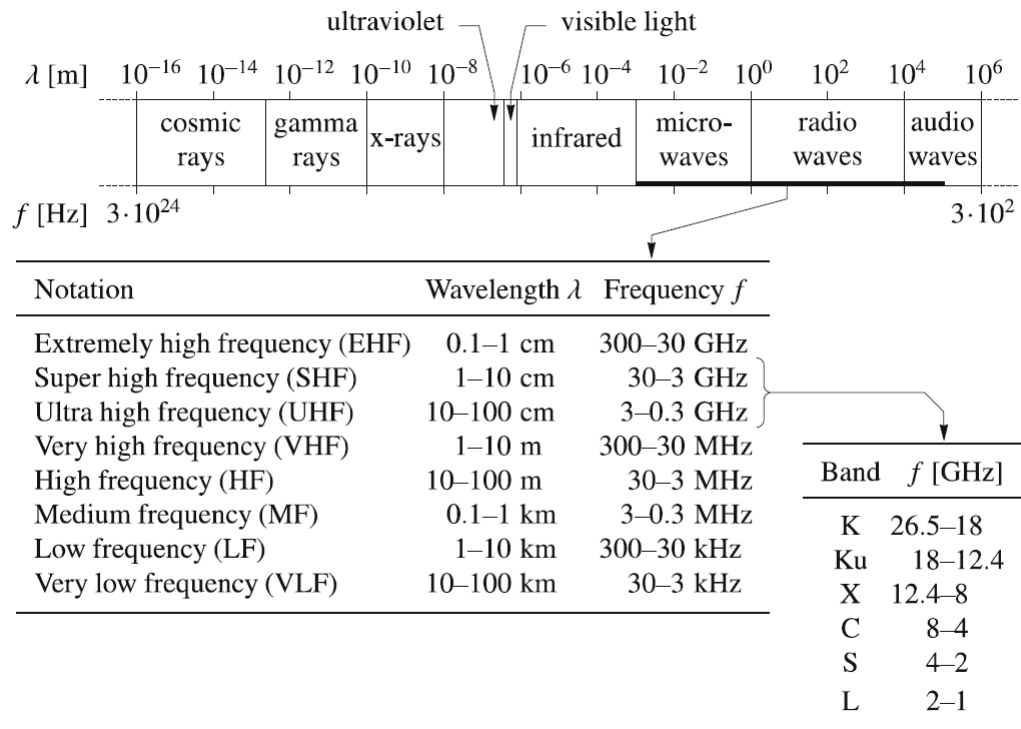


**Figure 2.2.** Electromagnetic spectrum (source: [4, p. 60]).

equals the ratio of the refractive indices of both media.

$$\frac{\sin(\beta_i)}{\sin(\beta_r)} = \frac{n_i}{n_r} = \text{constant}. \quad (2.2)$$

Figure 2.3 illustrates those two physical phenomena.

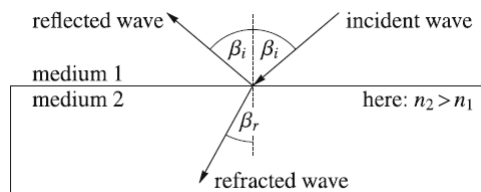


**Figure 2.3.** Reflection and refraction of an electromagnetic wave (source: [4, p. 61]).

Another factor influencing waves is absorption. Energy of a wave is converted into heat when propagating through a medium. It is correlated with frequency. The higher the frequency, the bigger absorption. Signal power is attenuating with increasing distance from the emitter.

All those effects influence satellite signals as they travel to receivers. The amount of energy transferred by the wave per unit time is expressed as power. Transmission loss,  $L$ , is described as a power ratio of the power measured at the receiver,  $P_r$ , to the power

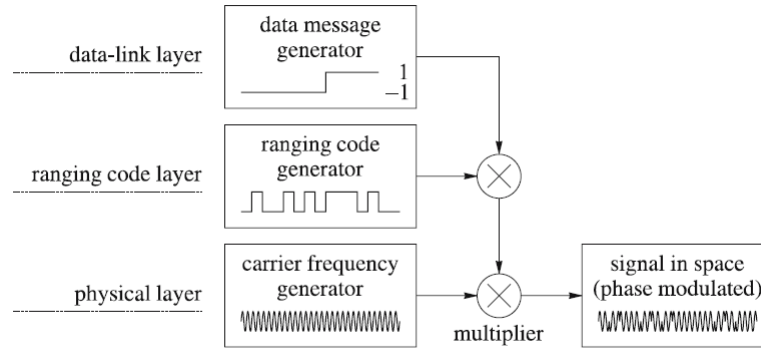


**Figure 2.4.** Signal composition (source: [4, p. 55]).

emitted from the satellite,  $P_s$ . It is given in decibel units and defined as:

$$L = 10 \log_{10} \frac{P_r}{P_s}. \quad (2.3)$$

#### 2.4.4 Satellite signal composition

Satellite signals can be represented by a three-layer model as illustrated in Figure 2.4. The physical layer generates a carrier wave with the frequency assigned by the ITU. As the name suggests, the carrier wave carries the navigational information. The navigational message contains parameters like time transmission and satellite ephemerides and is generated by the data link layer. The data message is modulated by the ranging code onto the carrier wave. The ranging code is a Pseudorandom Noise (PRN) code. It is a periodic sequence of rectangular pulses. PRN codes are unique for each satellite and allow interoperability of many satellites.

### 3 GNSS MEASUREMENTS

This chapter covers basic design principles of GNSS receivers and their measurements. Moreover, the differences between commercial and professional GNSS receivers are discussed. The chapter is mainly based on [4].

#### 3.1 Receivers

The function of GNSS receivers is to process signals coming from satellites. Even though, receiver's design strongly depends on a target application basic building blocks are common to all of them. Generic receiver architecture consists of antenna, radio front-end, digital signal processor, and navigation processor. Figure 3.1 shows the architecture.

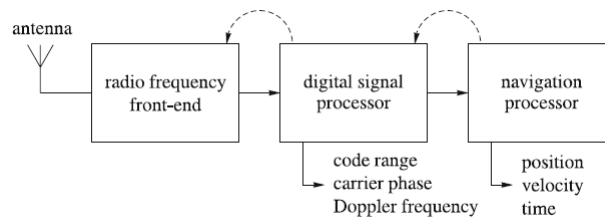


**Figure 3.1.** GNSS receiver (source: [4, p. 85]).

First, the antenna captures GNSS signals by converting energy from the electromagnetic waves into electric currents. Next, the radio front-end (RF) is responsible for signal conditioning which means signal preparation to meet the requirements of the next processing stage. The RF typically performs filtering, downconversion to the intermediate frequency, and the analog-to-digital conversion. Processing signals transmitted by moving satellites requires constant signal acquisition and tracking. When the receiver starts operating for the first time it does not have any information about its position, time or available satellites. Acquisition is the process of establishing which satellites are in view and can be tracked. It relies on a principle of signal correlation. Satellite PRN codes are known to the receiver, thereby it can generate local replicas of expected signals taking into account additional factors such as the carrier frequency, code delays, and the Doppler frequency. The incoming signals are repeatedly correlated with replicas. When the incoming signal aligns with the replica, the receiver starts the tracking process. The tracking loop continuously tracks the incoming signal and updates code delay and carrier phase parameters. The carrier phase describes the motion between the transmitter and the receiver and the code delay determines the mismatch between the local code replica and the satellite sig-

nal. These parameters are then used to update the local replica that is synchronized with the incoming signal. After synchronization the navigational message is demodulated and measurements are extracted by the digital signal processor (DSP) block. DSP correlates the locally generated signals with the incoming signal and generates measurements. The last block, the navigation processor, decodes the navigational message and calculates position, velocity and time information.

### 3.2 Observables

GNSS signals provide three types of measurements: pseudorange, carrier phase, and Doppler.

- Pseudorange ([4, pp. 105/106])

Subtracting emission time measured at the satellite,  $t_s$ , from reception time measured at the receiver,  $t_r$ , gives signal propagation time,  $\Delta T$ . This value multiplied by the speed of light gives us the apparent range between satellite and receiver. Due to asynchronicity of the satellite and receiver clocks and other delays it is not a precise geometric distance and is therefore called (code)pseudorange. The satellite clock bias and the receiver clock bias are termed  $\delta_s$  and  $\delta_r$  respectively.

$$\text{pseudorange} = c((t_r + \delta_r) - (t_s + \delta_s)) = c(\Delta T + \Delta \delta). \quad (3.1)$$

- Carrier phase ([4, pp. 106/108])

Carrier phase measurements express the difference between phases of the incoming carrier signals and their replicas generated by the receiver. When the receiver locks the satellite signal it can measure the initial fractional phase difference, but it cannot establish the whole number of cycles between satellite and receiver. As a result, the carrier measurement is ambiguous by an unknown integer number. If the signal is tracked without loss of lock the integer ambiguity remains the same. However, every time the receiver loses the lock on the signal, it loses the cycle count and the integer ambiguity changes. However, there are techniques resolving this problem. Ensuring constant integer ambiguity and common phase bias in all tracking channels enable usable carrier phase measurements that are typically two orders more precise than code pseudoranges.

- Doppler ([4, pp. 108/109])

The Doppler measurement is a change in the frequency caused by relative motion of the receiver and the satellite. The Doppler shift,  $f_D$ , is approximately given by:

$$f_D = f_r - f_t \approx f_t \left(1 + \frac{v}{c}\right), \quad (3.2)$$

where  $f_r$  is the received frequency,  $f_t$  is the transmitted frequency,  $v$  is the line-of-sight velocity of a satellite, and  $c$  is the speed of light. The Doppler shift is given in

Hertz, however, it is common to provide a pseudorange rate measurement in  $m/s$  which is a Doppler shift multiplied by the  $\frac{c}{f_c}$ , where  $c$  is the speed of light and  $f_c$  is the frequency of the carrier wave.

### 3.3 Signal strength

Signal-to-noise ratio (SNR), ([4, pp. 86/87]), is a measure indicating the strength of the signal. It is the ratio of the signal power,  $P_s$ , and noise power,  $P_n$ , in a given bandwidth and is usually expressed in decibels:

$$\text{SNR} = 10\log_{10}\frac{P_s}{P_n}[\text{dB}], \quad (3.3)$$

The logarithmic scale make it easier to analyze a large range of values. On the other hand, Carrier-to-noise ratio ( $C/N_0$ ) is a bandwidth-independent measure of signal strength. It is the ratio of the carrier power,  $C$ , and the noise power per unit bandwidth (noise power density),  $N_0$ , and is given in decibel-Hertz:

$$C/N_0 = 10\log_{10}\frac{C}{N_0}[\text{dB} - \text{Hz}], \quad (3.4)$$

$C/N_0$  is commonly used to determine the power of the received signal, whereas SNR can describe the performance of a receiver's functional block. Moreover,  $C/N_0$  is independent of the acquisition and tracking algorithms used by a receiver.

#### SNR variability

The SNR values can differ depending on a collection conditions, collection manner, hardware of a receiver or hardware of a satellite. This diversity can make SNR measurements non-comparable. In [3] authors used opportunistically crowd sourced GNSS data from heterogeneous mobile devices to detect and construct 3D representations of buildings. In addition, they provided a thorough analysis of collected SNR measurements. Their data was collected in an uncontrolled manner meaning users were not instructed where or how to carry the phone. Moreover, the data was collected by 900 distinct users of different Android devices.

To investigate the effect of different satellites hardware authors calculated a SNR histogram of six most seen satellites in their data. Satellites belonged to two different constellations (GPS and GLONASS) and to six distinct hardware revisions. Authors did a Kruskal-Wallis ([8]) test that showed no significant differences in SNR distributions. The Kruskal-Wallis test is a non-parametric method for testing whether samples originate from the same distribution. Thus, authors concluded that probably due to the common operation system of devices and similar GNSS chipsets data from different satellites does not require normalization.

Next, data from different smartphones was analyzed. Alike the previous test six smartphones of distinct brands were taken into consideration. Again, the Kruskal-Wallis test showed no significant difference in the SNR distributions. From this it could be concluded that smartphone chipsets calculate the SNR value similarly. However, some correlation between the SNR value and the satellite elevation was observed. For elevations lower than  $20^\circ$  authors observed a notable attenuation in average and maximum SNR value. For instance, the average SNR value for  $20^\circ$  and  $10^\circ$  elevation differed by 20%. The reason might be that signals from satellites near the horizon travel longer, through denser atmosphere and are more likely to be obstructed. Therefore, signals from elevations lower than  $10^\circ$  were excluded from the data set.

Another source of signal attenuation is caused by transient conditions or obstacles such as the local weather, passing vehicles or people. In this case, crowd sourced data has a big advantage thanks to the law of large numbers. As long as the data set is big enough and consists of enough distinct users the influence of transient obstacles is even out. In conclusion, [3] showed that crowd sourced data from low accuracy receivers collected in uncontrolled manner can be used to detect buildings.

### 3.4 GNSS receivers in smartphones

GNSS receivers can be divided into consumer-grade and professional-grade categories. Consumer-grade receivers are widely used in mobile devices such as smartphones, smartwatches, tablets, laptops, etc. High accuracy is not the primary requirement for those devices. Usually, an accuracy of a few meters is sufficient. For instance, when users want to check their position in the city they prefer less accurate localization within few seconds than waiting for a couple of minutes for a high, sub-meter accuracy. Hence, more important for consumer-grade devices are low-cost components, battery consumption optimisation, and positive user experience assured by among others short waiting time and availability.

On the other hand, professional-grade receivers are required to provide high accuracy, often within a meter or better, in all conditions. They are widely used for mapping, land surveying, measurements for building constructions, tracking, cargo monitoring, navigation, military, and many others. Taking those facts into account, consumer-grade receivers significantly differ from professional-grade ones.

The first difference between the two categories of GNSS receivers is the antenna. Inexpensive smartphone antennas employ linear polarization as opposed to high quality devices with circular polarization. The satellite signal is a circularly polarized wave. Circular polarization consist of two orthogonal linear polarized waves with a  $90^\circ$  phase difference. Because linearly polarized antennas receive only the in-phase component of the circular wave they have the polarization mismatch loss of 3dB. Secondly, antenna's directivity can attenuate some signals. Directivity is the measure of the concentration of an antenna's radiation pattern in a particular direction. Additionally, typical smartphone design

forces the antenna to be installed in a place that does not prevent the user to adversely influence it. Often users' hands cover up antenna and that can considerably weaken the signal reception. According to [9], antenna's linear polarization and directivity account for loss in the signal's power of around 11 dB. Next, to limit battery consumption smartphones use the duty cycle technique that leads to carrier phase tracking discontinuity. This discontinuity does not allow for the use of the advanced positioning techniques such as Real Time Kinematic (RTK) or Precise Point Positioning (PPP) and as a consequence it adversely influences the positioning accuracy. According to [9] only 60% of data from a smartphone with active duty cycle was valid for RTK or PPP.

Furthermore, mobile navigation chipsets use Assisted-GNSS (A-GNSS) architecture, which allows lowering the waiting time of a service. The Time To First Fix (TTFF) is a time required for a device to acquire satellite signals and navigation data, and calculate its position. TTFF depends on the start up of the device. There are three types of start-ups: cold, warm, and hot. The cold start is when a receiver does not have any information and needs to obtain the ephemeris data to calculate its position. It can take 30 seconds or more. At the warm start, a receiver remembers time, its last calculated position, and almanac data. It only needs to obtain the available satellite signals. Finally, the hot start is when a receiver knows time, almanac, last position, and all satellites in view. It is the quickest start and usually takes up to a couple of seconds. The A-GNSS utilizes smartphone built-in communication devices such as cellular network modem and WiFi. Therefore, a mobile receiver can get approximate position and time based on cellular network positioning. Moreover, the A-GNSS provides the assistance data including ephemeris, clock corrections and ionospheric models available for mobile devices through wireless networks. The A-GNSS enables mobile devices to establish their first fix within a few seconds and it improves the accuracy in harsh environments. However, several radio modules embedded inside relatively small smartphones can cause interference and worsen their performance.

### **3.5 Android raw measurements**

Nowadays, smart devices, especially smartphones, are widely used in our daily life. In 2019 at the I/O developer conference Google announced that there were around 2.5 billion active devices with the Android operating system. Since 2016 Android 7.0 Nougat has provided access to raw GNSS measurements. It allowed developers to directly use carrier and code measurements and decoded navigation messages from smart devices. The availability of raw measurements created an opportunity for improving accuracy of positioning algorithms and development of innovative solutions such as combining GNSS and sensor data.

In [2] authors assessed the quality of GNSS observations from Android N devices. They compared measurements from a tablet and a geodetic-quality antenna and receiver. Devices used in this experiment were a consumer-grade tablet HTC Nexus 9 and a

professional-grade NovAtel receiver. The  $C/N_0$  reflects gains and losses of a signal power along the transmission chain. Authors of the study compared an average  $C/N_0$  of satellites with respect to their elevation angle. Satellites observed within an elevation range of  $2^\circ$  were grouped together and the average of their  $C/N_0$  was calculated. The study showed that  $C/N_0$  measured with the tablet were approximately 10 dB-Hz lower than measurements from NovAtel. Moreover, the standard deviation of smartphone's  $C/N_0$  values was two to three times higher than from the geodetic receiver. Hence, the smartphone data is more unstable and sensitive to obstructions. In conclusion, smartphone  $C/N_0$  values showed larger variability and vulnerability to interference than values from NovAtel.

## 4 DISRUPTIONS

This chapter describes three types of signal disruptions: interference, signal blockage and multipath. The chapter is mainly based on [5].

### 4.1 Interference

Interference happens when two waves traveling through a common communication channel superpose and form a new wave with a greater, lower, or same amplitude. In case of GNSS systems it is caused by radio signals from any undesired source and results in degraded navigation accuracy or complete loss of satellite tracking. Interference can be unintentional or intentional. Unintentional interference can be caused by other services relying on the L-band frequency. Moreover, some influence from the signals in adjacent bands cannot be avoided. On the other hand, intentional interference is a deliberate attempt to deteriorate GNSS signals. Three categories of intentional interference can be distinguished: jamming, spoofing, and meaconing. Jamming attacks aim to overpower GNSS signals so that they cannot be acquired and tracked. Spoofing is an action to purposely produce untrue position, velocity, or time of the receiver by generating false GNSS-alike signals. Meaconing is a rebroadcast of navigation signals in order to confuse a navigation system and produce untrue positions.

### 4.2 Signal blockage

Signal blockage (also called signal masking or shadowing) occurs when a radio signal encounters a physical obstacle. As a result, signal can weaken or be totally absorbed or reflected. Signal attenuation strongly depends on the type of the obstacle. It can be vegetation, terrain or a man-made structure.

Vegetation usually includes trees either with dense or sparse foliage. In addition, vegetation's impact is also dependent on with humidity and wind. As stated in [10] vegetation with foliage causes signal attenuation 24%-35% bigger than vegetation with no foliage.

Terrain is the second type of obstacles. Its influence on signals varies a lot due to changing terrain profile. However, physical models of terrain can be used to predict signal behavior. The Terrain-Integrated Rough-Earth Model (TIREM) ([11]) enables to forecast signal propagation losses over irregular terrain.

The most relevant blockage type to this work are men-made structures such as buildings. Propagation losses considerably differ depending on building shape, structure and used materials.

Results from [10] also showed that attenuation declines with higher elevation angles of a satellite. Figure 4.1 visualizes the phenomenon.

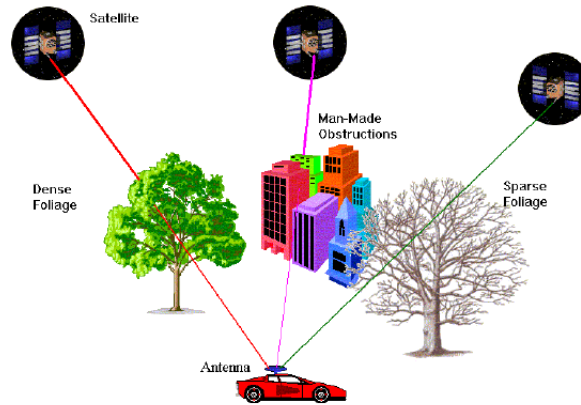


**Figure 4.1.** Signal blockage (source [12]).

### 4.3 Multipath

Multipath is the reception of reflected or diffracted replicas of the direct path signal. The satellite signal arrives to the receiver by more than one path. It is caused by reflective surfaces encountered by the signal. The effect is illustrated in Figure 4.2. The reflected (non-line-of-sight (NLOS)) signal travels a longer path than the direct (line-of-sight (LOS)) signal so its arrival is delayed. If the delay is big the receiver can distinguish it and reject the signal. However, short delays are more difficult to identify and can be problematic.

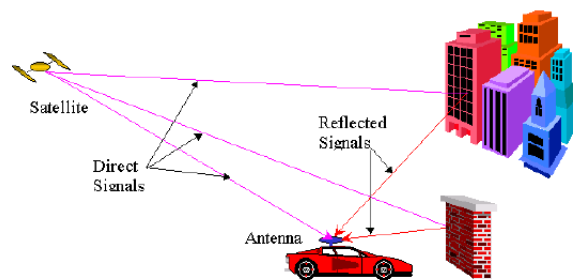


**Figure 4.2.** Multipath (source [12]).

### 4.4 Shadow matching

GNSS services tend to perform poorly in urban areas. High buildings and narrow streets create urban canyons in which signals from many satellites are shadowed or reflected. The number of available direct LOS signals drops and so NLOS signals must be used to

calculate user position, which results in deteriorated accuracy. At the same time, cities are densely populated and the demand for GNSS services is high. In [1] authors proposed a shadow matching algorithm that deals with the urban canyon issue and improves positioning accuracy in urban areas. Authors took advantage of increasing availability of accurate 3D models of cities to enhance positioning performance. Based on a 3D model they estimated satellite visibility in a considered location and predicted which satellite signals were shadowed by buildings. Then, they compared predictions with real observations and could for example distinguish on which side of the road the user was located.

Figure 4.3 depicts the shadow matching concept. Let us consider a satellite and a user receiving its signal as on the left illustration of Figure 4.3. Based on the 3D model we can determine where the signal will be shadowed. Then, if the user receives the signal and it is strong and direct we can improve positioning accuracy and specify that the user is on the right side of the street. The idea of using 3D models to establish satellite visibility is essential to this thesis and it was a starting point for the thesis concept.

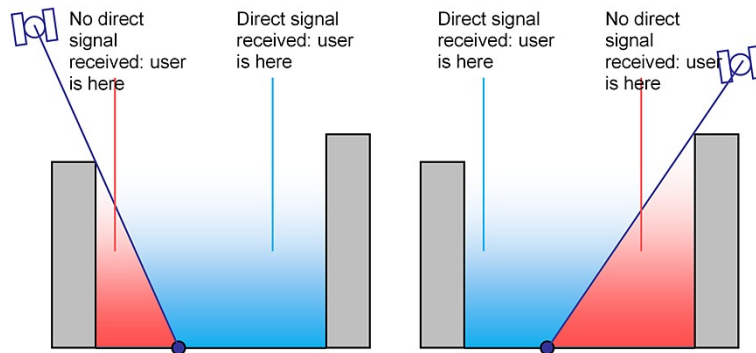


**Figure 4.3.** Shadow matching (source [1]).

## 5 DATA ANALYSIS

In this chapter data collection, processing, and analysis are described.

### 5.1 Data collection

In the experiment two Xiaomi MI 8 smartphones equipped with Broadcom BCM47755 chip were used. The chip is a dual-frequency GNSS receiver, which means it can simultaneously compute signals from two frequencies: L1 and L5. The receiver supports following signals: GPS L1/L5, Galileo E1/E5a, GLONASS L1, BeiDou L1, and QZSS L1/L5. Dual frequency ensures higher accuracy and higher resistance to multipath and interference. Smartphones were installed in a test car. One phone was placed on the dashboard and one on the roof. Moreover, the car was provided with NovAtel ProPak6 receiver ([13]) installed in the trunk. NovAtel ProPak6 includes a functionality that integrates inertial measurements to provide a high-rate, continuous navigation solution. Figure 5.1 shows the set up. Table 5.1 presents formats and software used to process collected data.

The experiment was conducted in the city center of Tampere. The test route contained several places in which we expected to observe a missing map element. The Tampere City Unity 3D City Model (source: [14]) provided 3D map data. It was created based on Open GIS data and The City of Tampere planning documents. The 3D city model was prepared in the Unity engine in GK24FIN coordinate system. The elements of the 3D model were provided as FBX files.

Data collection was carried out on one day at different hours. In total the route was driven four times. The GNSSLogger app that is available on Android devices served to collect the raw observables from smartphones in a form of text log files. NovAtel binary logs were converted to RINEX Observation File format with NovAtel Convert dedicated software. In addition, NovAtel receiver was used to log precise coordinates of the car during the test. Those coordinates were used as ground truth locations of devices and the file containing them is later referred to as the reference file. Reference locations were represented in WGS84 datum.



(a) Test car



(b) Smartphone on the roof



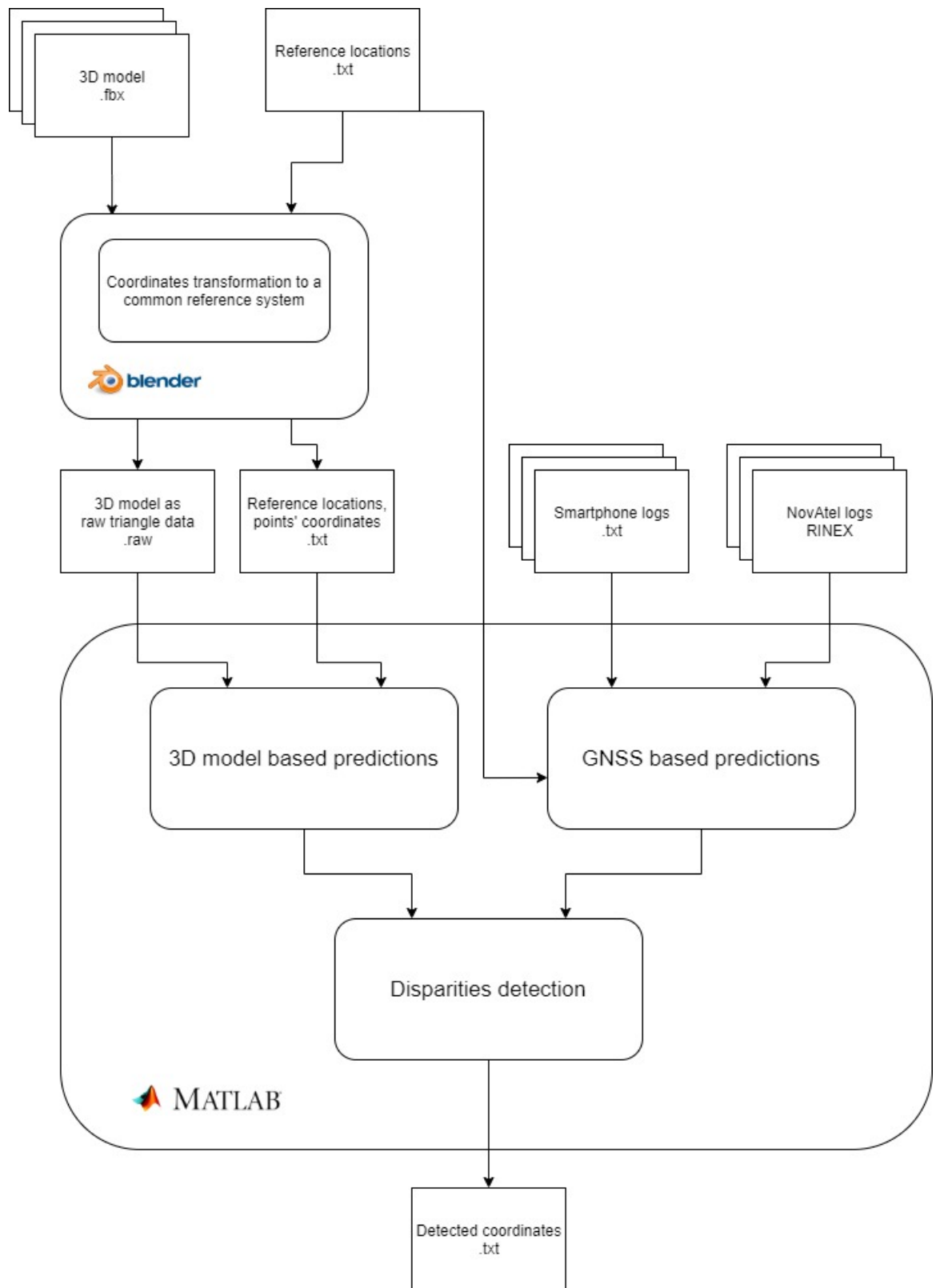
(c) Smartphone on the dashboard

**Figure 5.1.** Device installation.

## 5.2 Data processing

Data processing and implementation of an algorithm were done using Matlab and Blender. Figure 5.2 presents a block diagram of data processing steps. The GNSSLogger app provides text log files containing raw GNSS observations. Each raw observation contains among others a timestamp, constellation ID, satellite ID, and  $C/N_0$ . The reference file contains among others timestamps, latitudes, longitudes, altitudes, and north and east velocities. Timestamps of raw GNSS observations were matched with reference timestamps, which allowed to associate GNSS data with the geographic coordinates. Since smartphones and NovAtel were collecting data simultaneously the exact timestamps could be matched. As a result, satellites observed at each location were known. NovAtel observation file contains among others timestamps, satellite ID, constellation ID, and  $C/N_0$ . The same association of GNSS observations and locations was applied to the NovAtel observation files.

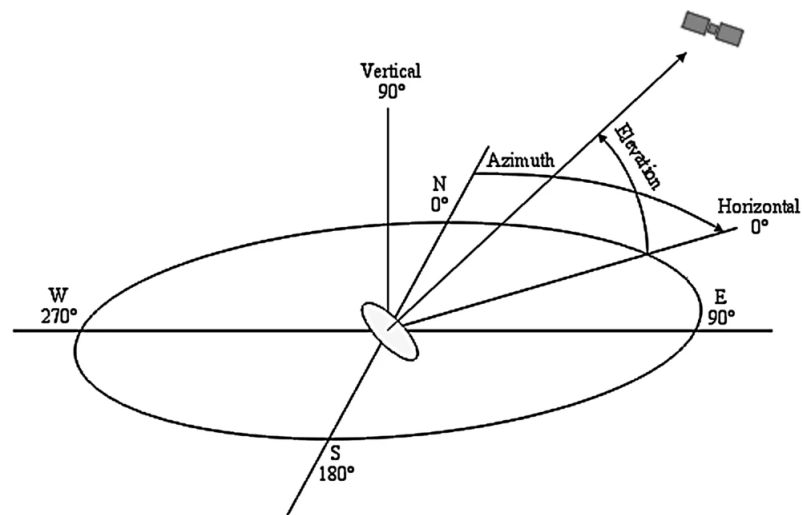
Next, the azimuth and elevation angles for each observed satellite were calculated. The angles can be calculated if the satellite ID, the constellation, the location of the receiver, and the ephemeris data were known. The broadcast ephemeris data is openly available for download for example from NASA's server. Azimuth is the clockwise angle between a satellite and the North. Elevation is the angle between the horizontal plane and the line of sight, measured in the vertical plane. Figure 5.3 illustrates the angles.



**Figure 5.2.** Block diagram of data processing.

**Table 5.1.** Software and data formats.

format	version	description	specification
RINEX	3.03	Data interchange format for raw satellite navigation system data	[15]
FBX	-	Proprietary file format providing interoperability between digital content creation applications formats.	[16]
software	version	description	reference
Matlab	R2019b	Multi-paradigm numerical computing environment and proprietary programming language developed by MathWorks.	[17]
Unity	2017.3.1f1	Cross-platform game engine developed by Unity Technologies.	[18]
Blender	2.79	Free and open-source 3D computer graphics software toolset.	[19]
GNSSLogger	2.0.0.1	Android app allowing registering for various Android location related measurements.	[20]
NovAtel Convert	2.6.3	Software converting NovAtel logs.	[21]

**Figure 5.3.** Satellite's azimuth and elevation (source [22]).

### 5.2.1 3D-model based predictions

3D models in computer graphics are commonly represented with a triangle mesh. The triangle mesh is a type of mesh where all objects are defined as a set of connected

triangles. Blender can export model's objects to raw triangle mesh data where each triangle is defined as  $(x, y, z)$  coordinates of its three vertices. Figure 5.4 illustrates an example building represented with a triangle mesh.

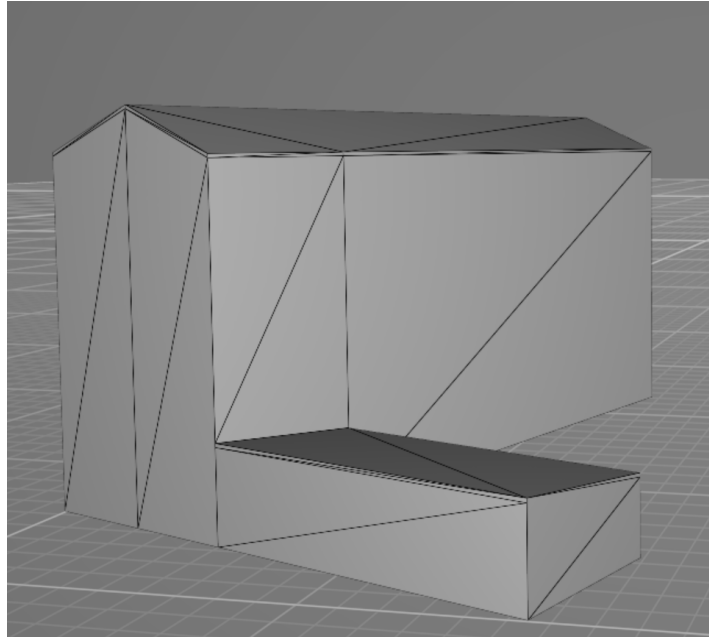


**Figure 5.4.** Building represented with a triangle mesh.

To check whether a signal at a certain location is shadowed by a building the reference geographical coordinates were imported into the 3D model. Reference locations were first transformed to GK24FIN coordinate system and then formed a path. Afterwards, the path was exported as  $(x,y,z)$  coordinates of its points.

Next step was to determine, for each path point, at which azimuth and elevation a satellite signal is blocked by 3D model's objects. This question can be represented as the ray-triangle intersection problem. [23] provides comprehensive introduction to ray tracing algorithms. The Möller–Trumbore ray-triangle intersection algorithm presented in [24] that computes the intersection of a ray with a triangle was used. In this case, a satellite signal is a ray that is represented as vector defined in spherical coordinates. The spherical vector is described with  $(r, \theta, \phi)$  where  $r$  is the length of the vector,  $\theta$  ( $0 \leq \theta \leq 90^\circ$ ) is the angle between the positive Z-axis and the vector, and  $\phi$  ( $0 \leq \phi \leq 360^\circ$ ) is the angle between the projection of the vector onto the X-Y-plane and the positive X-axis. Then, for each  $\theta$  and  $\phi$  with  $5^\circ$  resolution the existence of intersections with model's triangles was checked. If the intersection exists then the ray is considered blocked. The search area was narrowed down to lower the computation cost by filtering the model data to include only triangles within reasonable distance from the considered path point.

This calculation was done for all path points so that for each point it was known at which  $\theta$  and  $\phi$  the incoming signal would be blocked. Figure 5.5a shows an example path point and its surrounding in the 3D model. Plot 5.5b shows predictions of blocked angles at that point. Red crosses correspond to blocked angles and blue circles to not blocked angles.

It can be seen that due to surrounding buildings on the right and left side angles on the sides are blocked. In contrast, angles at the top and bottom of the plot are not blocked because of lack of obstacles.

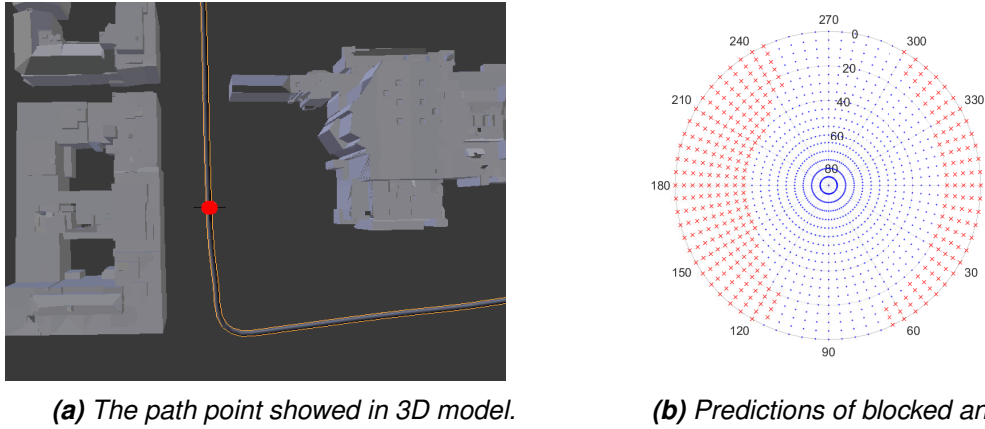


**Figure 5.5.** 3D model-based predictions of blocked angles at a certain path point.

### 5.2.2 GNSS-based predictions

GNSS-based predictions were based on a fundamental observation that the power of a satellite signal significantly decreases when the signal crosses a building. This section examines measurements of signals' power based on the data collected in Tampere.

#### $C/N_0$ analysis

Firstly, the mean value of  $C/N_0$  measurements in respect to the elevation angles was calculated. Then outcomes from smartphones and the NovAtel were compared. As can be seen in Figure 5.6, there is around 10 db-Hz difference between mean values from smartphones and NovAtel, which is consistent with the results from [2] as described in 3.5. Generally, it can be seen that the higher elevation angle the higher  $C/N_0$  mean value. The  $C/N_0$ 's dependency on the elevation angle agrees with the findings of [3]. Also, the mean value from smartphones for  $10^\circ$  elevation is significantly lower than mean values for higher elevations. Therefore, for further processing observations from satellites with elevations lower than  $15^\circ$  were excluded from our data.

Next, mean  $C/N_0$  values of all GPS satellites from smartphone data were calculated. The results are shown in Figure 5.7, which shows big variability of mean values. It was caused by the fact that during data collection some satellites were visible only at low elevations and some satellites only at high elevations. On the contrary to the huge amount of data described in 3.3 our data set was relatively small. Data was gathered on one day at two different hours (the route was driven twice starting at each hour), hence it did not contain observations from all possible locations of satellites on the sky. Figure 5.8 shows two skyplots at two hours of data collection. The figure shows only GPS satellites for better clarity. Skyplots illustrate initial satellite locations and trajectories of movements.

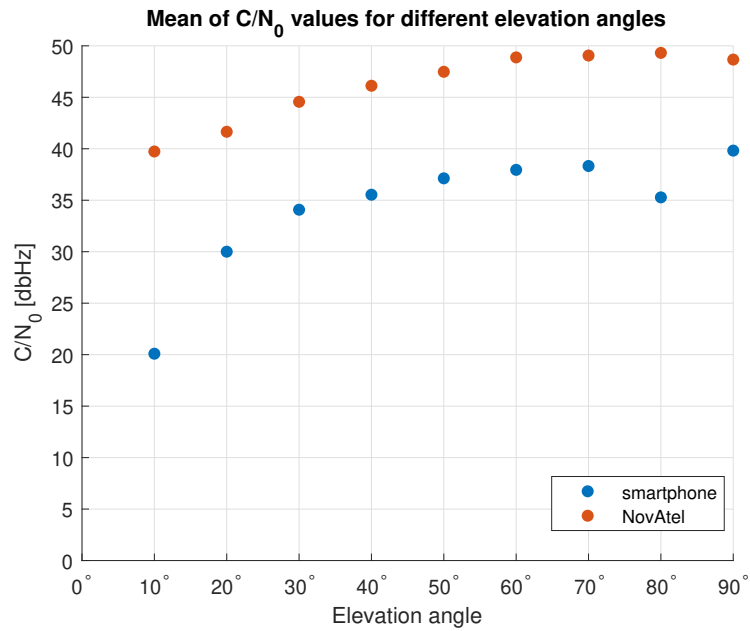


**Figure 5.6.** Comparison of mean  $C/N_0$  values from smartphones and NovAtel for different elevation angles.

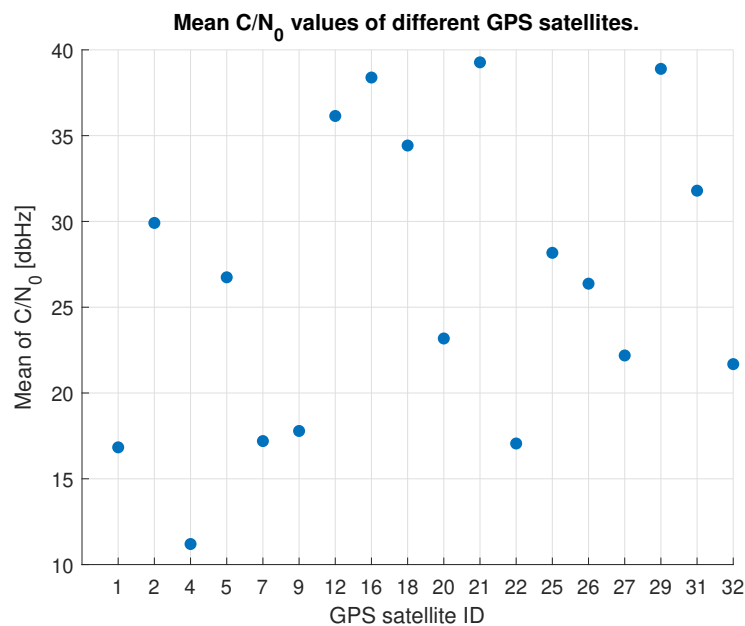


**Figure 5.7.** Comparison of mean  $C/N_0$  values of different GPS satellites.

For instance, between the first and the second collection round the satellite G29 traveled from azimuth around  $220^\circ$  and elevation around  $60^\circ$  to azimuth around  $95^\circ$  and elevation around  $70^\circ$ .

Figure 5.9 presents  $C/N_0$  values of a GPS21 satellite over time collected by the smartphone and the NovAtel. According to the corresponding skyplot GPS21 was at elevation above  $60^\circ$  degrees, which explains high  $C/N_0$  value. Smartphone observations fluctuate more than NovAtel's observations, therefore smartphones are more susceptible to disruptions. Moreover, at around 15:12 there is a notable drop. It was caused by a railway



overpass on the route, that in fact is a short tunnel cutting off all satellite signals. The difference is that NovAtel's  $C/N_0$  value dropped to zero while smartphone's  $C/N_0$  value dropped by approximately 30 dB-Hz. So NovAtel receiver is more accurate and reports zero value when a satellite is not observed.

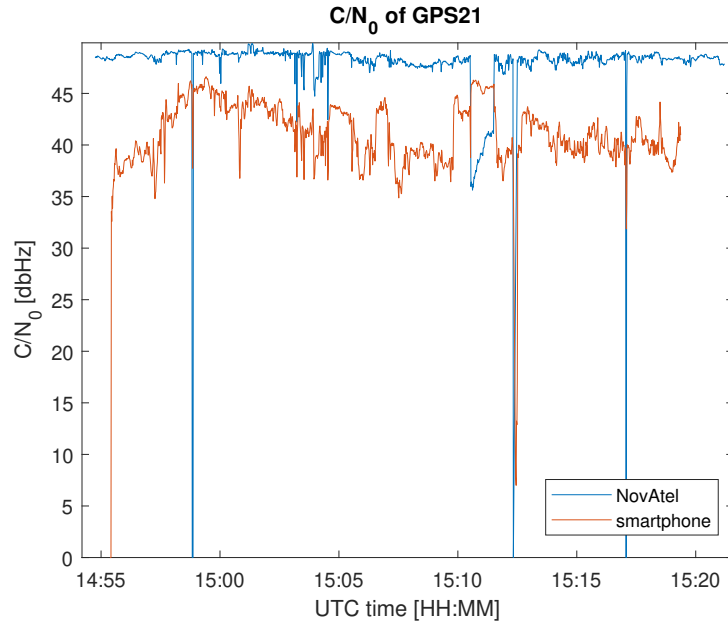


**Figure 5.9.**  $C/N_0$  values of GPS21 satellite over collection time.

However, GPS21 was an example of a satellite with the high mean  $C/N_0$  value. Other satellites at lower elevations had more noisy and scattered  $C/N_0$  values. To compare, Figure 5.10 shows data from the smartphone and the NovAtel of GPS5 at elevation  $30^\circ$ . GPS5 signal had  $C/N_0$  at a lower level and signal's fluctuations were much bigger than fluctuations of GPS21's signal. Moreover, it can be seen that the NovAtel was often losing GPS5 signal and logged its value as zero.

To sum up, to predict whether a signal is blocked or not a threshold  $C/N_0$  value below which signal is assumed to be blocked needed to be specified. In [1] signals with  $C/N_0$  below 40 dB-Hz were treated as weak signals. However, due to big variability of  $C/N_0$  of different satellites in the data collected for the purpose of this work each satellite was considered separately and a different threshold for each of them was assigned. In this work a signal was treated as blocked if its  $C/N_0$  value dropped by 20 dB-Hz or more. Therefore, a threshold was obtained by subtraction of 20 dB-Hz from a maximum  $C/N_0$  value of a satellite.

### 5.3 Reality Index

The next step of the algorithm was to compare 3D model and GNSS based predictions of the satellite visibility and detect possible errors in the 3D model. The test route included places where new buildings, not yet present in the model, were built. The algorithm was expected to detect those locations as wrongly mapped. Moreover, the route included one

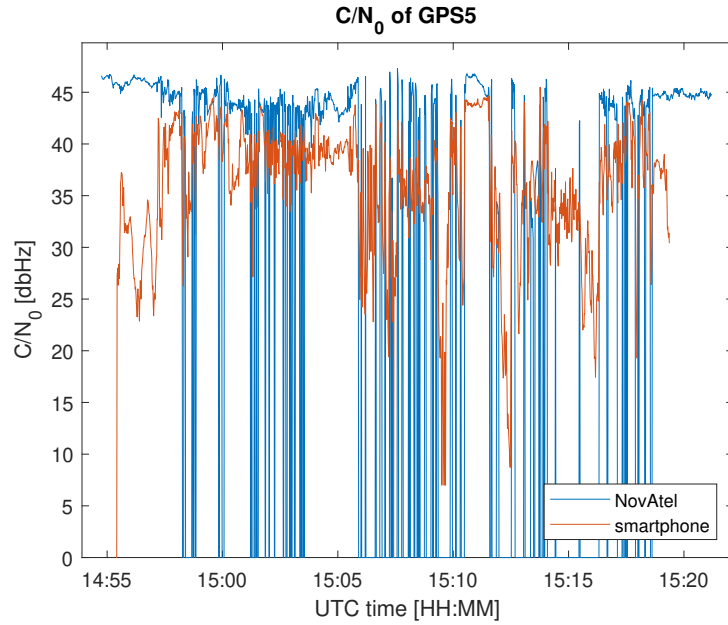


**Figure 5.10.**  $C/N_0$  values of GPS5 satellite over collection time.

bridge and one railway overpass (short tunnel) that blocked all possible satellite signals due to the total blockage of the sky view. Those two elements were not included in the model as well since the model covered only buildings. To detect errors in the 3D model a reality index that showed the probability of the error was defined. The reality index (RI) was calculated for each reference location. The 3D model and GNSS based predictions of all visible satellites in a location were compared. The reality index was a ratio of number of satellites which predictions matched to a total number of observed satellites. Therefore, the fewer matched predictions the lower reality index. Also, if there were less than four observed satellites the reality index was not calculated due to insufficient data and the reference location was skipped. The reality index is formulated by equation 5.1.

$$RI = \frac{SV_{matched}}{SV_{observed}}, SV_{observed} \geq 4, \quad (5.1)$$

- $SV_{matched}$  - number of satellites whose 3D-model and GNSS based predictions matched
- $SV_{observed}$  - number of observed satellites

In addition, for more precise results satellites on the right and on the left side of the vehicle were divided and the reality index for both sides was calculated separately. This was possible thanks to NovAtel's reference file that contained north and east velocities of the vehicle. Based on those velocities it was possible to calculate a direction where the vehicle was heading and then determine the relative positions of satellites. To reflect the real road situation where usually the vehicle drives along the street and buildings are on the sides the sky plot was divided as shown in Figure 5.11. The final reality index for a location combined the right and the left side results. If either of them was less than or

equal to 0.5 the error in the 3D model was reported.

$$\text{Error detection} = \begin{cases} 1, & \text{if } (RI_{\text{right}} \leq 0.5) \text{ or } (RI_{\text{left}} \leq 0.5). \\ 0, & \text{otherwise.} \end{cases} \quad (5.2)$$

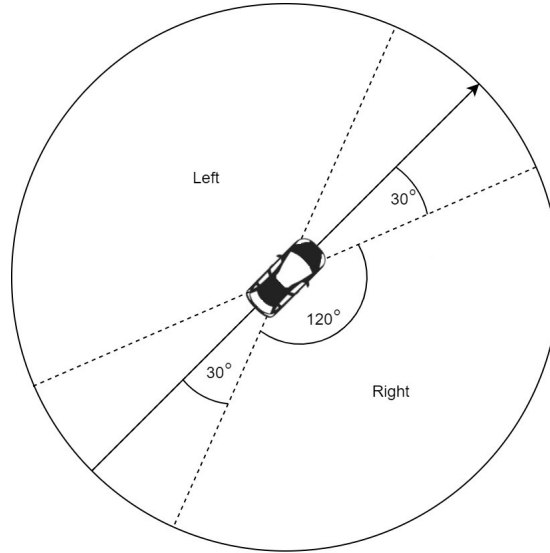


**Figure 5.11.** Division of the sky view.

## Results from the NovAtel

Firstly, let us analyze results from one of the NovAtel logs. Figure 5.12 shows the reality index plot. Yellow markers correspond to correctly mapped locations, whereas dark red and dark blue markers indicate errors in the 3D model. Dark red color indicates places where the model is missing elements and dark blue color indicates places where model contains extra elements. The following part is an analysis of selected errors. Errors in the figure were numbered to make the description easier.

Error number one indicates an extra element in the 3D model that does not exist in reality. Figure 5.13a shows the satellite image of considered location and its corresponding 3D model. We can see that, in fact, there is an additional building, that is not visible in the satellite image.

Error number two is a group of locations that reported mismatch of predictions. They are caused by the characteristics of the terrain surrounding the street. On both sides of the street there is an embankment with trees. It blocks satellites from lower elevations. Figure 5.14a shows the sky plot in one of the discussed location. Blue circles and red crosses represent 3D model based predictions of not blocked and blocked angles respectively. Diamonds represent satellites observed by the receiver. Green satellites are not blocked and black are blocked according to GNSS measurements. The yellow dot marker represents vehicle's heading. On the left side black satellites on blue background cause the error. According to 3D model satellites should not be blocked, but because of the terrain,

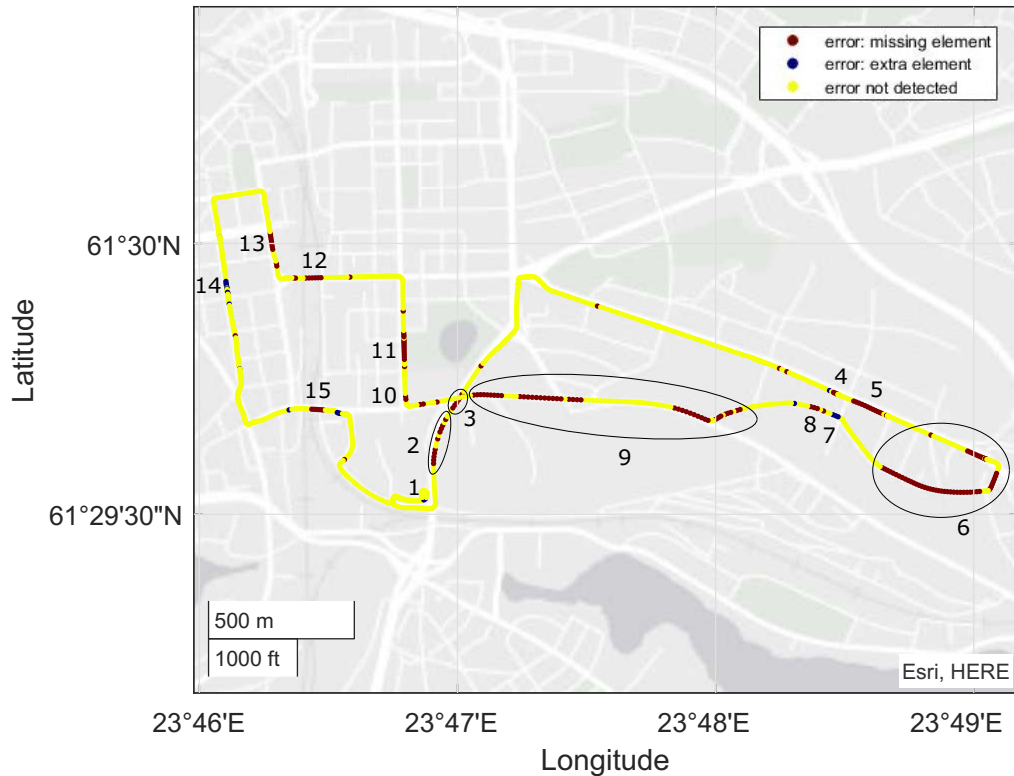


**Figure 5.12.** Reality Index based on the NovAtel log file.

that is not included in the 3D model, the actual signals are blocked.

Next, error number three is caused by the bridge. When the vehicle was underneath it satellite signals were cut off. In Figure 5.14b we can see blocked satellites. However, the bridge was not included in the model so predictions were different, and the error was detected. A similar situation happened when the car drove under the railway overpass and it is reflected in the error number twelve.

Figure 5.13b shows the satellite image of location number four and its corresponding 3D model. On the right image there are red and two yellow rectangles representing missing and modified buildings in the 3D model respectively. Moreover, 5.14c shows the sky plot in the considered location. We can see two mismatched satellites due to the lack of the building in the model and one mismatched satellite due to an extra obstacle.

On the satellite photo 5.13c we can see a construction site. However, at the time of data collection there were three high blocks of flats. On the contrary, the 3D model contained the old building, hence the mismatch presented in figure 5.14d. According to GNSS measurements four satellites were blocked but because the correct building did not exist in the model the error was reported.

Next error, number six, is located in an area that was redeveloped. Old buildings were replaced with new residential houses. Moreover, in the bottom of satellite image 5.13d there is a dense forest whose part was cutout and a new building was built. All those changes were responsible for reported errors. New building were blocking signals that

were not predicted to be blocked.

Error number seven correctly detected an extra building in the model. Recently demolished building was still present in the model. Figure 5.13e shows the area and 5.14e shows the sky plot. In the bottom of the sky plot there are three mismatched satellites due to additional building in the model.

Error number eight is caused by the left-most building in the picture 5.13b of the model. Satellites were blocked by the new higher building and reported missing element in the model.

Error number nine is a group of mismatches spread along the street, that is not in direct proximity to buildings. However, it is surrounded by high trees on both sides that caused unwanted signal blockage.

Another error, number ten, is caused by a newly built hotel. It is shown in Figure 5.13f and Figure 5.14f shows corresponding sky plot. Satellites on the right side are in deed blocked by the hotel but model predictions do not reflect it and cause the error.

Next wrongly mapped area is shown in the 5.13g. The model is missing a building on the left side of the street. Figure 5.14g shows predictions. Again, we can observe that satellite signals are blocked but 3D model predictions are different.

Error number thirteen is shown in Figure 5.13h. The building on the right side of the street was modified. An additional part was added on top of the front part and a new block added in the back. The higher front part of the building, that is not included in the model, blocks satellites shown in the sky plot 5.14h and causes the mismatch.

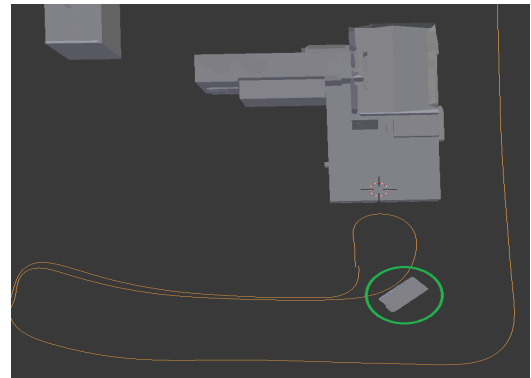
Next, error number fourteen indicates an extra building in the model. Sky plot 5.14i shows that satellites on the right side should be blocked but their GNSS measurements say otherwise. However, in this case buildings are correctly mapped. The reason of the error is the multipath effect. Satellite signals are reflected by the high building from the opposite side of the street. Therefore, the device still receives these signals. Error number fifteen is caused by a construction site of a new sport arena that blocks signals.

## **Results from the smartphone**

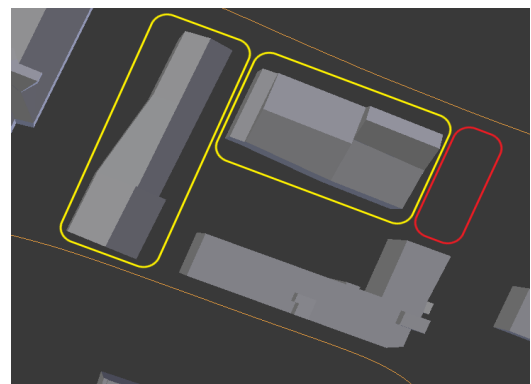
Next, let us analyze results from one of the smartphone's logs. Figure 5.15 presents the reality index plot. As can be seen smartphone's results differ significantly from NovAtel's results. The majority of reported errors concern extra elements in the model. However, some errors detected based on smartphone data coincide with NovAtel's results. Smartphone's errors number one, three, five, six and ten agree with Novatel's errors number one, six, seven, eleven and twelve respectively. Next, the rest of smartphone's errors were analyzed.

Error number two is connected to the bridge. However, it was only detected in one location and the sky plot 5.16a shows that significantly fewer satellites than in NovAtel result

were predicted to be blocked. Drive time under the bridge was probably too short for the smartphone to react and recognize more satellites as blocked.

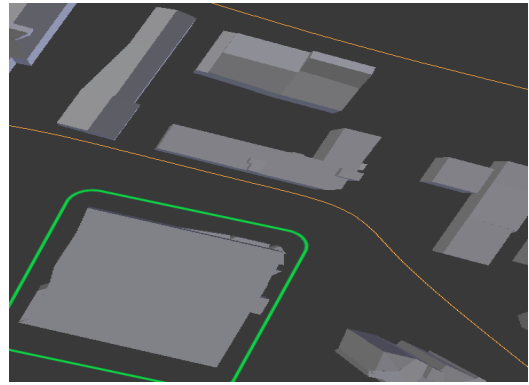


(a) NovAtel - error 1

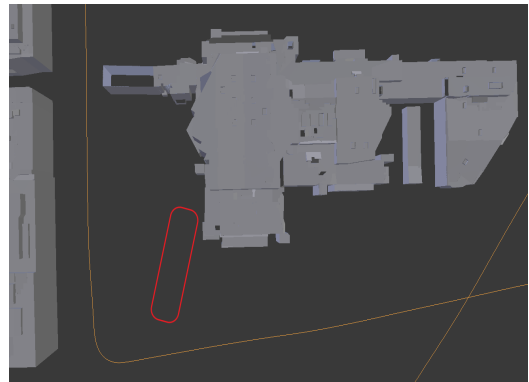
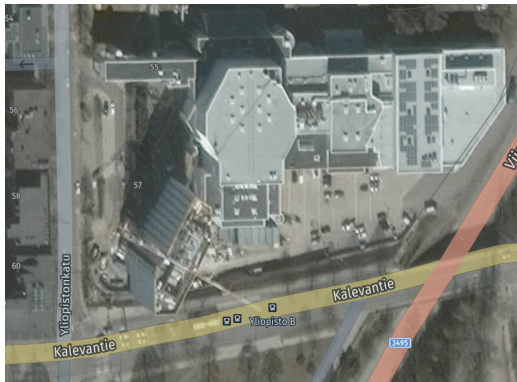


(b) NovAtel - error 4

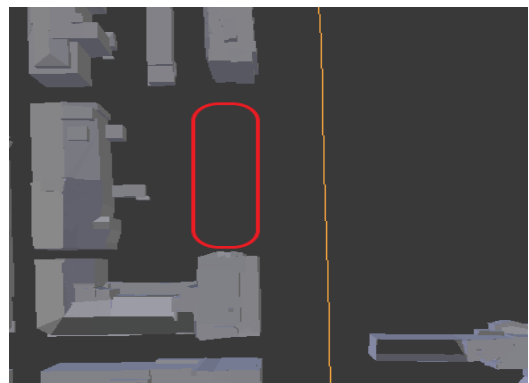




(e) NovAtel - error 7



(f) NovAtel - error 10



(g) NovAtel - error 11

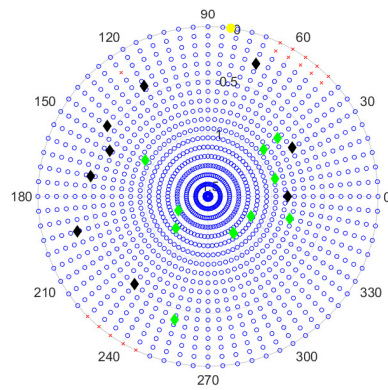


(h) NovAtel - error 13

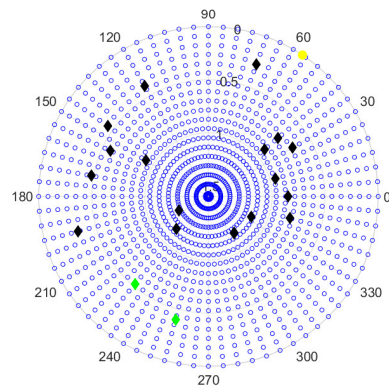
**Figure 5.13.** Satellite images of discussed areas in the left column (source [26]) and their corresponding 3D models in the right column.

Errors number four, seven, eight, eleven and twelve were caused by the same reason. All those places were surrounded by high buildings reflecting signals causing multipath. GNSS based predictions recognized satellites as visible despite surrounding buildings that blocked them. It caused the mismatch and resulted in false errors. In this case buildings were correctly mapped but GNSS predictions were incorrect. Figures 5.16b, 5.16c, 5.16d, and 5.16f show those wrong predictions.

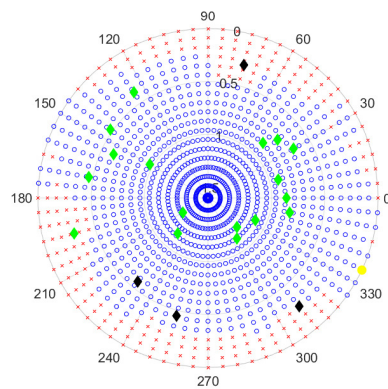
Error number nine indicates a missing building in the model. There is in deed a modified building that blocks signals and cause the error.



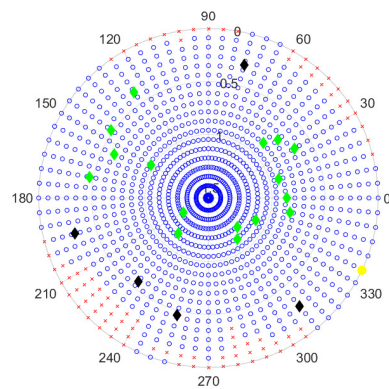
**(a) NovAtel - error 2**



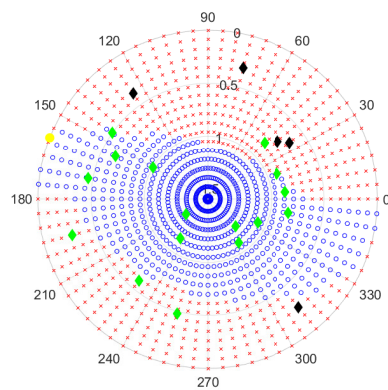
**(b) NovAtel - error 3**



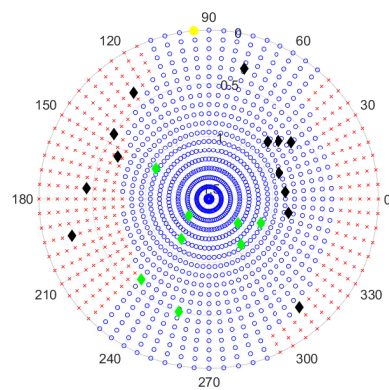
**(c) NovAtel - error 4**



**(d) NovAtel - error 5**



**(e) NovAtel - error 7**



**(f) NovAtel - error 10**

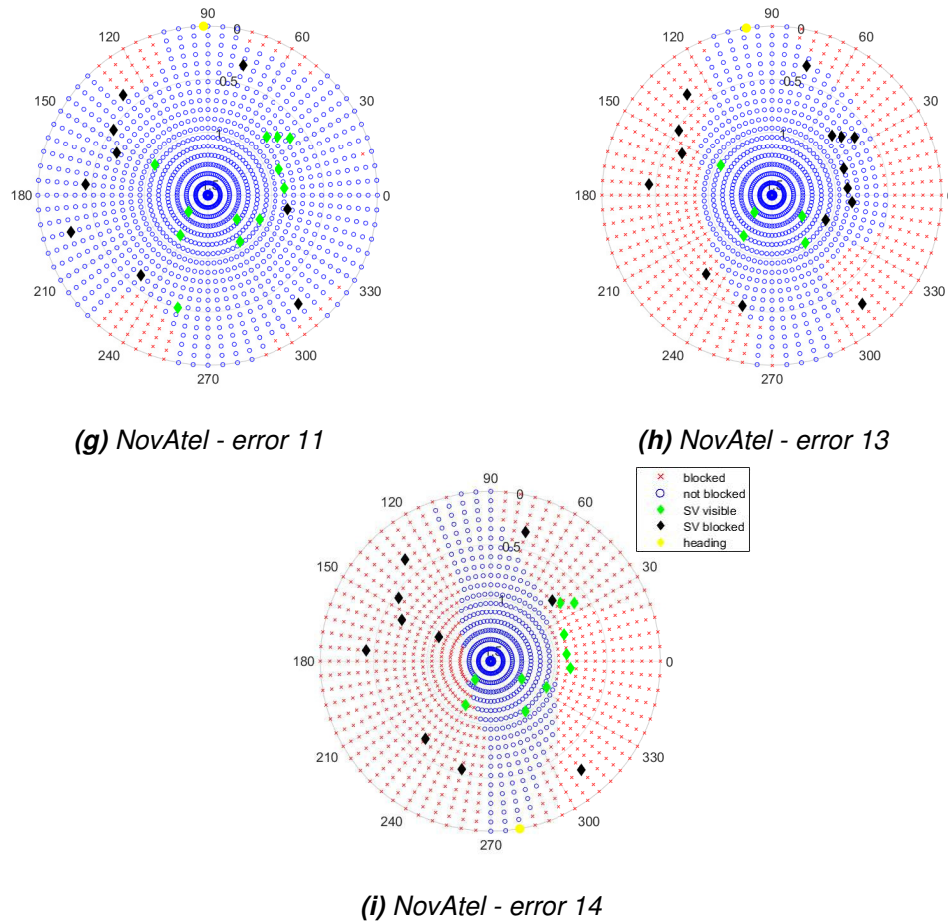


**Figure 5.14.** Sky plots comparing 3D model and GNSS based predictions from the NovAtel in discussed locations.

## Results from combined files

Next, results from multiple log files from the same device type (NovAtel or smartphone) were combined and examined. Files were collected at different hours so that satellite locations were different and they could account for detections of various errors in the model. Moreover, if an error was detected in all log files the probability of its validity would be higher. Results from multiple files were combined in the following way. If results from more than half of files reported an error it was taken into account, otherwise the error was dismissed. Figures 5.17 and 5.18 show combined results from Novatel's and smartphones' logs respectively. In the case of Novatel combined results eliminated the false error number fourteen but otherwise they do not significantly differ from the single file results. Elimination of the above mentioned error using combined results proves that merging results from many satellites at different locations can give more reliable results. Similarly combined smartphones' results, detected generally the same places as the single file results.

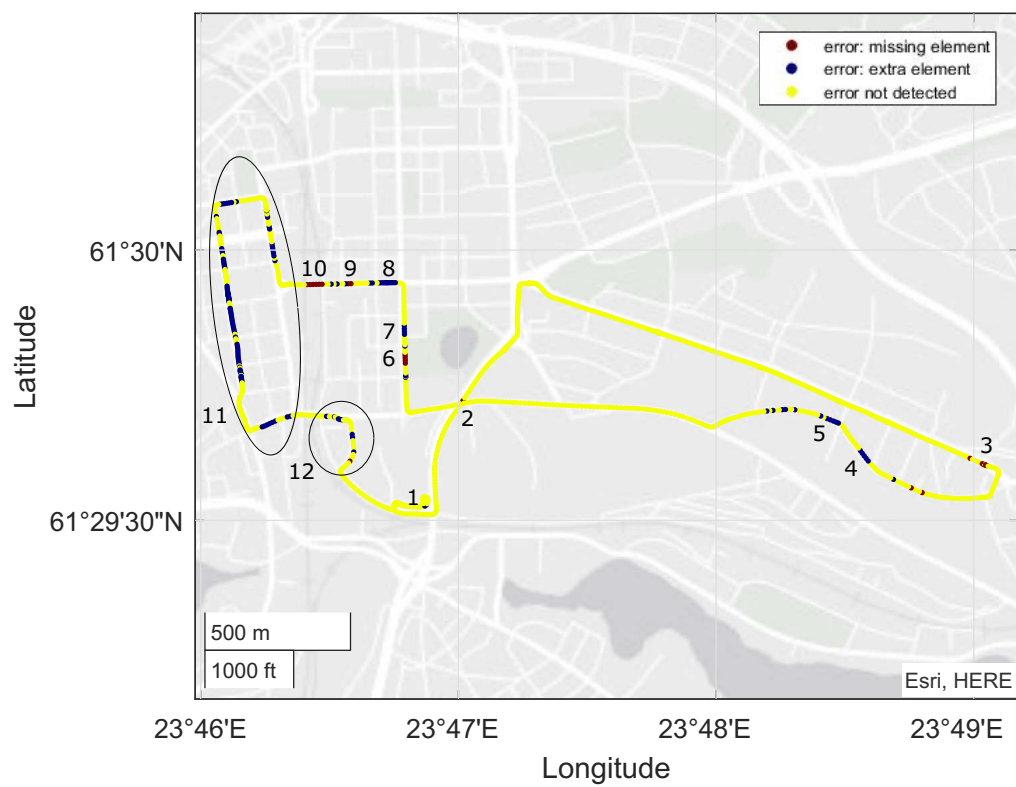
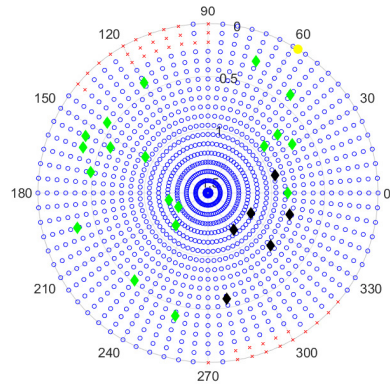
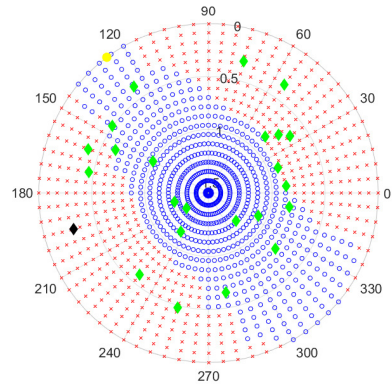


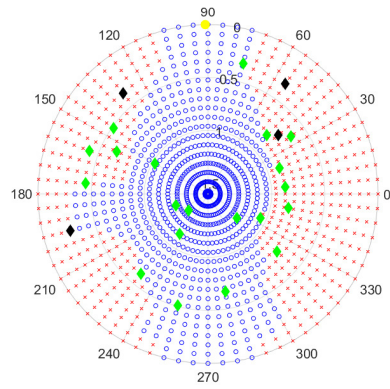
**Figure 5.15.** Reality Index based on the smartphone log file.



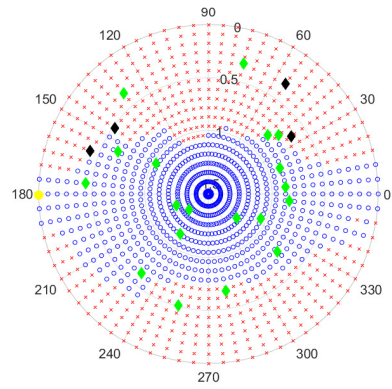
(a) Smartphone - error 2



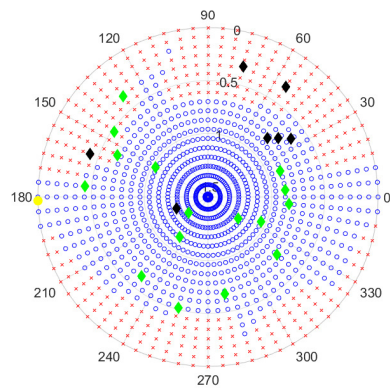
(b) Smartphone - error 4



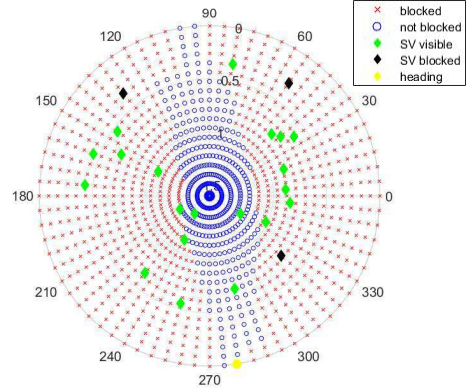
(c) Smartphone - error 7



(d) Smartphone - error 8



(e) Smartphone - error 9



(f) Smartphone - error 11

**Figure 5.16.** Sky plots comparing 3D model and GNSS based predictions from the smartphone in discussed locations.

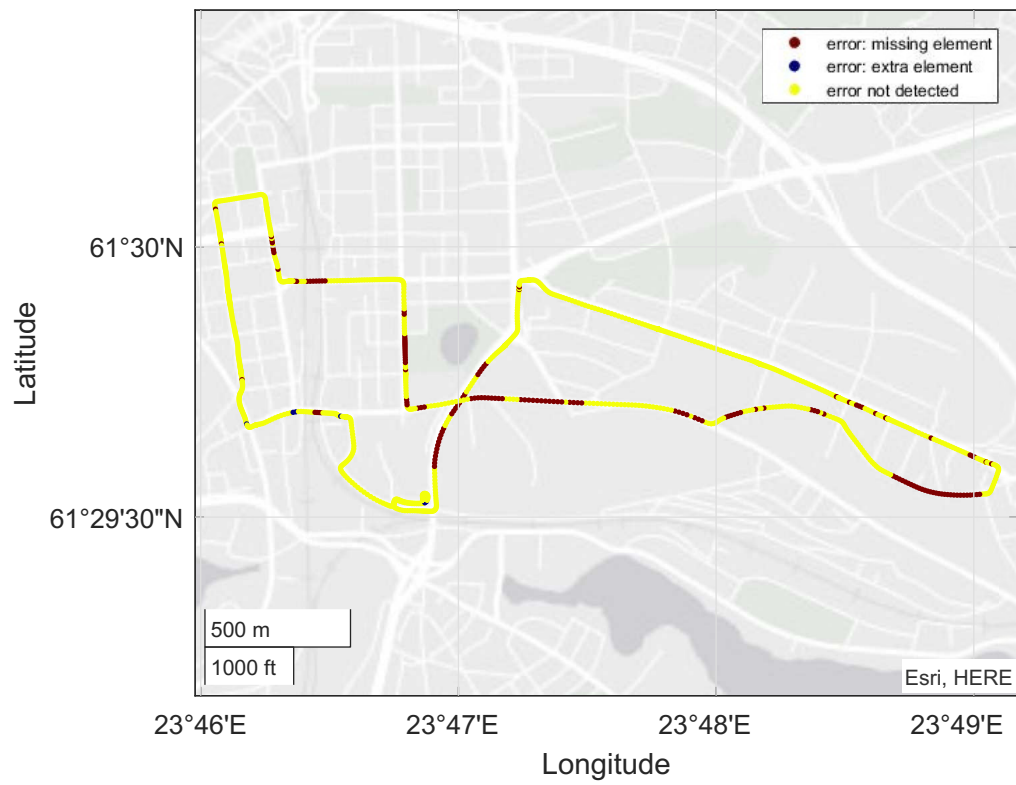


**Figure 5.17.** Reality Index based on combined NovAtel's log files.

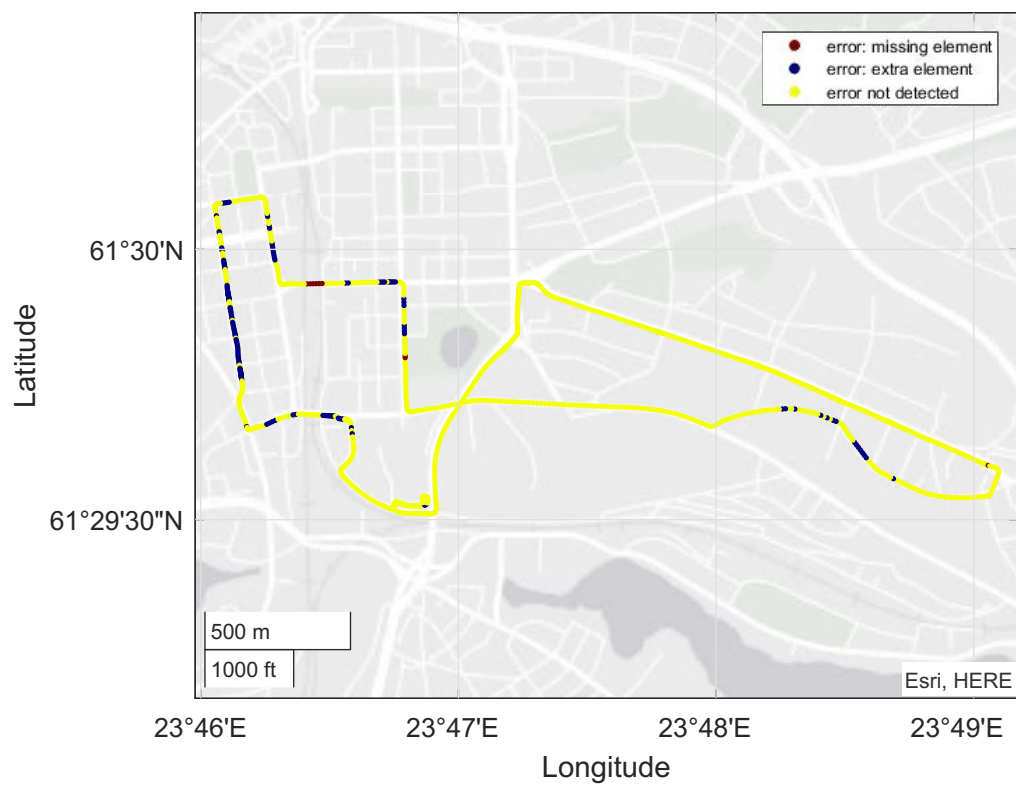


**Figure 5.18.** Reality Index based on combined smartphones' log files.

## 6 CONCLUSIONS

The goals of the thesis were to validate the 3D model using raw GNSS observations and to verify whether smartphones' receivers are sufficient for that purpose. To validate the correctness of the 3D model predictions of satellites visibility based on 3D model and GNSS measurements were compared. GNSS measurements were collected using smartphones and the professional grade NovAtel receiver for reference. The data collection route included places wrongly mapped in the 3D model that were expected to be detected. Table 6.1 summarizes number of detected errors based on the Novatel and smartphone single log files. NovAtel correctly detected twice as many errors as the smartphone. Moreover, smartphone did not detected six errors and detected five false errors.

A GNSS measurement, Carrier-to-noise ratio ( $C/N_0$ ), was used to distinguish blocked satellite signals. The analysis confirmed the fundamental assumption that signal power considerably decreases when blocked by an obstacle. It also showed the  $C/N_0$  dependency on the satellite's elevation angle. The lower the elevation angle the lower the  $C/N_0$  value. More precisely based on smartphone data the mean  $C/N_0$  value from satellites at elevations lower than  $15^\circ$  were around 15 db-Hz lower than mean  $C/N_0$  value from other satellites. This dependency is caused by longer travel distance through denser atmosphere and higher probability of signal obstruction. Comparison of  $C/N_0$  values from smartphones and the Novatel showed that smartphone measurements are on average 10 db-Hz lower than Novatel. Moreover, smartphones do not react to signal obstructions as quickly and as accurately as NovAtel. It was observed that NovAtel's  $C/N_0$  value immediately drops to zero when a signal is blocked while smartphone's  $C/N_0$  value only dropped by tens of db-Hz. To sum up, considering  $C/N_0$  measurements smartphones are less accurate than NovAtel, however, they reflect signal blockage and can be used to identify blocked signals.

The implemented algorithm compared 3D model and GNSS based predictions of blocked satellites and returned the reality index for each considered location telling the probability

**Table 6.1.** Summary of errors detection

	correctly detected	missed	incorrectly detected
NovAtel	14	0	1
Smartphone	7	6	5

of the error. Based on collected data the algorithm detected not only the expected errors but also more wrongly mapped buildings that were unknown due to insufficient knowledge of the city. Novatel successfully detected missing bridge, railway overpass and a couple of buildings. The extra elements and modified buildings were detected as well. In addition, the results were influenced by the terrain and trees that were not contained in the 3D model. On the other hand, NovAtel detected one false error caused by the multipath effect. In the considered location high buildings on both sides of the street reflected satellites signals and even though they were blocked the device received them with high  $C/N_0$  value. Furthermore, the multipath effect was a particular problem for smartphones. Smartphones' reality index results differed from NovAtel's. Smartphone did not detect all of the expected errors and due to multipath they detected many false errors. However, some places such as bridge, railway overpass, and some buildings were detected despite relatively small data set. In conclusion, the algorithm detected some errors in the 3D model. It recognized whether there was a missing or an extra element. However, it is not resistant to multipath effect and happens to result in false errors, especially with the smartphone data.

Our data set contained only data collected in one day at two different hours. Consequently, the data set did not consist of measurements from satellites at many different locations. On the other hand, the detection of buildings heavily depends on the satellites distribution on the sky. If there are no satellites in a particular area then there is no information about possible error and it can not be detected. Using data with more coverage of the sky plot would give more reliable results. In our case combined results from multiple files did not improve the outcomes because the data set was still too small to notice any enhancements. However, there are reasons to believe that much bigger data set would eliminate encountered issues. For instance in [3] it was shown that crowd sourced mobile data can be used to detect buildings.

For further research collecting or crowd sourcing more mobile data would provide better evaluation of smartphone usability. In addition, studying how to mitigate the multipath effect would improve the results. Other GNSS measurements, besides  $C/N_0$ , could assist in recognizing blocked signals. For example multipath affects pseudoranges and could be incorporated into the algorithm. Because a satellite signal is reflected by an obstacle and then reaches a receiver it travels a longer distance and so the pseudorange is bigger. Another improvement could be using more detailed 3D model containing terrain and vegetation.

## REFERENCES

- [1] Wang, L., Groves, P. D. and Ziebart, M. K. GNSS shadow matching: Improving urban positioning accuracy using a 3D city model with optimized visibility scoring scheme. *NAVIGATION: Journal of The Institute of Navigation* 60.3 (2013), 195–207.
- [2] Zhang, X., Tao, X., Zhu, F., Shi, X. and Wang, F. Quality assessment of GNSS observations from an Android N smartphone and positioning performance analysis using time-differenced filtering approach. *Gps Solutions* 22.3 (2018), 70.
- [3] Rodrigues, J. G. and Aguiar, A. Extracting 3D Maps from Crowdsourced GNSS Skyview Data. *The 25th Annual International Conference on Mobile Computing and Networking*. 2019, 1–15.
- [4] Hofmann-Wellenhof B. Lichtenegger H., W. E. *GNSS – Global Navigation Satellite Systems. GPS, GLONASS, Galileo, and more*. Springer-Verlag Wien, 2008.
- [5] Kaplan E., H. C. *Understanding GPS: Principles and Applications*. Artech House, 2017.
- [6] *An introduction to GNSS: GPS, GLONASS, Galileo and other Global Navigation Satellite Systems*. NovAtel Inc., 2015.
- [7] Yuanxin Wu, Ping Wang and Xiaoping Hu. Algorithm of Earth-centered Earth-fixed coordinates to geodetic coordinates. *IEEE Transactions on Aerospace and Electronic Systems* 39.4 (2003), 1457–1461.
- [8] Kruskal-Wallis Test. *The Concise Encyclopedia of Statistics*. New York, NY: Springer New York, 2008, 288–290. DOI: 10.1007/978-0-387-32833-1\_216. URL: [https://doi.org/10.1007/978-0-387-32833-1\\_216](https://doi.org/10.1007/978-0-387-32833-1_216).
- [9] Using GNSS Raw Measurements on Android Devices. *[European GNSS Agency]* (2017).
- [10] Goldhirsh J., V. W. J. Handbook of Propagation Effects for Vehicular and Personal Mobile Satellite Systems: Overview of Experimental and Modeling Results. (1998).
- [11] *TIREM*. URL: <https://www.alionscience.com/terrain-integrated-rough-earth-model-tirem/>. (accessed: 07.2020).
- [12] MacGougan G. Lachapelle G., N. R. Overview of GNSS Signal Degradation Phenomena. (2001).
- [13] *NovAtel ProPak6 product sheet*. URL: <https://hexagondownloads.blob.core.windows.net/public/Novatel/assets/Documents/Papers/ProPak6-PS-D18297/ProPak6-PS-D18297.pdf>. (accessed: 06.2020).
- [14] Kaupunkimittaus. *Unity 3D City Model of the City of Tampere. Under the license Creative Commons Attribution 4.0*. URL: [https://data.tampere.fi/data/en\\_GB/dataset/tampereen-kaupungin-unity-3d-kaupunkimalli](https://data.tampere.fi/data/en_GB/dataset/tampereen-kaupungin-unity-3d-kaupunkimalli).

- [15] *RINEX*. URL: <ftp://igs.org/pub/data/format/rinex303.pdf>. (accessed: 06.2020).
- [16] *FBX data format*. URL: <https://www.autodesk.com/products/fbx/overview>. (accessed: 06.2020).
- [17] *Matlab*. URL: <https://se.mathworks.com/products/matlab.html>. (accessed: 06.2020).
- [18] *Unity*. URL: <https://unity.com/>. (accessed: 06.2020).
- [19] *Blender*. URL: <https://www.blender.org/>. (accessed: 06.2020).
- [20] *GNSSLogger Android App*. URL: <https://github.com/google/gps-measurement-tools>. (accessed: 06.2020).
- [21] *Novatel Convert*. URL: <https://portal.hexagon.com/public/Novatel/assets/Documents/Downloads/Zips/NovAtelConvertSetup>. (accessed: 06.2020).
- [22] Mukesh, R., Karthikeyan, V., Soma, P. and Sindhu, P. Analysis of signal strength, satellite visibility, position accuracy and ionospheric TEC estimation of IRNSS. *Astrophysics and Space Science* 364.11 (2019), 196.
- [23] Glassner, A. S. *An introduction to ray tracing*. Elsevier, 1989.
- [24] Möller, T. and Trumbore, B. Fast, minimum storage ray-triangle intersection. *Journal of graphics tools* 2.1 (1997), 21–28.
- [25] *Trimble*. URL: <https://www.gnssplanning.com/#/skyplot>. (accessed: 06.2020).
- [26] *HERE Maps*. URL: <https://wego.here.com>. (accessed: 06.2020).